Article

Cell Reports

Thermodynamic and Evolutionary Coupling between the Native and Amyloid State of Globular Proteins

Graphical Abstract

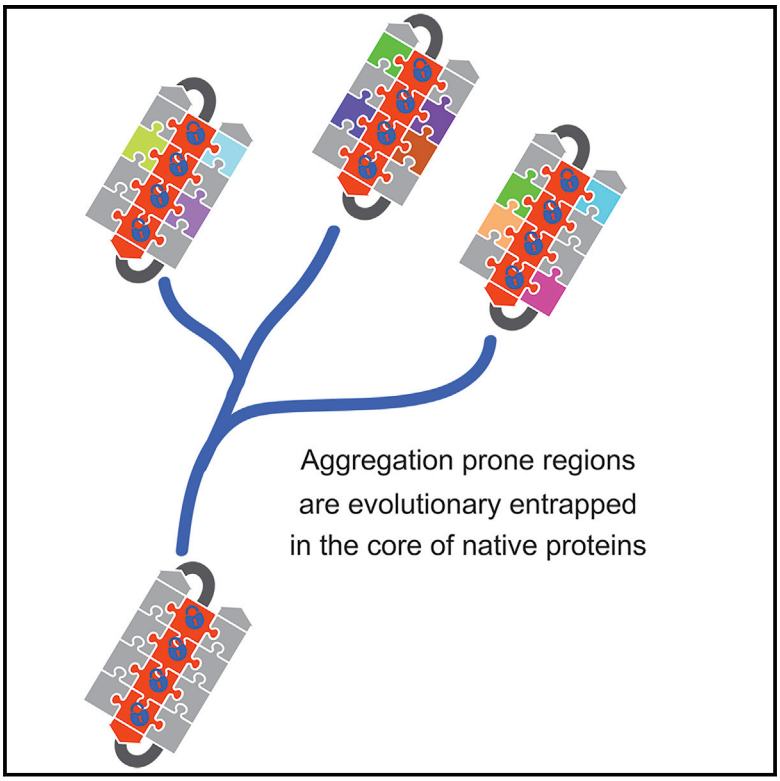

Authors

Tobias Langenberg, Rodrigo Gallardo, Rob van der Kant, ..., Joost Van Durme, Frederic Rousseau, Joost Schymkowitz

Correspondence

frederic.rousseau@kuleuven.be (F.R.), joost.schymkowitz@kuleuven.be (J.S.)

In Brief

Langenberg et al. show that amyloid propensity favors protein stability. This results from the energetic correlation of mutation in the native and amyloid state. The genetic code tightens this relationship so that stable amyloidogenic sequences are deeply conserved. Positive selection of amyloidogenic sequences could therefore have favored the evolution of globular structure.

Highlights

- Mutations in the globular and amyloid state are thermodynamically correlated
- The genetic code tightens this relationship between the amyloid and native state
- Strongly amyloidogenic sequences in globular proteins are deeply conserved
- Positive selection of amyloid propensity will favor globular protein stability

Langenberg et al., 2020, Cell Reports *31*, 107512
April 14, 2020
https://doi.org/10.1016/j.celrep.2020.03.076

CellPress

Cell Reports
Article

Thermodynamic and Evolutionary Coupling between the Native and Amyloid State of Globular Proteins

Tobias Langenberg,[1,2,4] Rodrigo Gallardo,[1,2,4,5] Rob van der Kant,[1,2] Nikolaos Louros,[1,2] Emiel Michiels,[1,2] Ramon Duran-Romaña,[1,2] Bert Houben,[1,2] Rafaela Cassio,[1,2] Hannah Wilkinson,[1,2] Teresa Garcia,[1,2] Chris Ulens,[3] Joost Van Durme,[1,2] Frederic Rousseau,[1,2,6,*] and Joost Schymkowitz[1,2,*]

[1]Switch Laboratory, VIB Center for Brain and Disease Research, Herestraat 49, 3000 Leuven, Belgium
[2]Switch Laboratory, Department of Cellular and Molecular Medicine, KU Leuven, Herestraat 49, 3000 Leuven, Belgium
[3]Laboratory of Structural Neurobiology, Department of Cellular and Molecular Medicine, KU Leuven, Herestraat 49, 3000 Leuven, Belgium
[4]These authors contributed equally
[5]Present address: Astbury Centre for Structural Molecular Biology, School of Molecular and Cellular Biology, University of Leeds, Leeds LS2 9JT, UK
[6]Lead Contact
*Correspondence: frederic.rousseau@kuleuven.be (F.R.), joost.schymkowitz@kuleuven.be (J.S.)
https://doi.org/10.1016/j.celrep.2020.03.076

SUMMARY

The amyloid-like aggregation propensity present in most globular proteins is generally considered to be a secondary side effect resulting from the requirements of protein stability. Here, we demonstrate, however, that mutations in the globular and amyloid state are thermodynamically correlated rather than simply associated. In addition, we show that the standard genetic code couples this structural correlation into a tight evolutionary relationship. We illustrate the extent of this evolutionary entanglement of amyloid propensity and globular protein stability. Suppressing a 600-Ma-conserved amyloidogenic segment in the p53 core domain fold is structurally feasible but requires 7-bp substitutions to concomitantly introduce two aggregation-suppressing and three stabilizing amino acid mutations. We speculate that, rather than being a corollary of protein evolution, it is equally plausible that positive selection for amyloid structure could have been a driver for the emergence of globular protein structure.

INTRODUCTION

The Anfinsen postulate states that protein folding is a thermodynamically determined process and, thus, that all of the information required to adopt the native conformation is encoded in the amino acid sequence of a protein (Anfinsen, 1973; Anfinsen and Haber, 1961). For most proteins, however, this principle is embedded in a more complex reality dictated by physico-chemical constraints on protein folding kinetics and thermodynamics. Local structural propensities can conflict with the native state conformation, resulting in structural frustration (Dill et al., 2008). These local versus global structural contradictions are a source of protein misfolding and lead to less efficient protein folding. For some proteins, this results in folding kinetics that are too complex to be resolved without the help of molecular chaperones (Horwich et al., 1990; Jayaraj et al., 2020). A major form of structural frustration is the tendency of local sequence fragments to form intermolecular interactions with the identical sequence fragment of another protein chain by β strand association, resulting in formation of amyloid-like assemblies (Iadanza et al., 2018).

Amyloid assembly is therefore a competitive side reaction of protein folding that significantly affects folding efficiency and requires a significant amount of metabolic energy to avoid aggregation (Landreh et al., 2016). It is not only detrimental to protein function, but the amyloid conformation is also associated with toxic gain of function in a range of degenerative pathologies (Dobson et al., 2020). It is therefore considered that the high aggregation propensity of proteomes across all kingdoms of life is a negative side effect of globular protein structure and their requirement of a hydrophobic core (Ganesan et al., 2016; Rousseau et al., 2006). As discussed above, this strained relationship between protein stability and aggregation led to a redefinition of the Anfinsen postulate, where the native folding landscape is in competition with a second aggregation-determining energetic landscape (Jahn and Radford, 2008). These competing landscapes are characterized by very different structural topologies that are dominated by different non-covalent interactions (Iadanza et al., 2018). The amyloid conformation is a multimolecular assembly that is dominated by backbone-backbone interactions, whereas the globular structure is generally a monomolecular conformation that is predominantly stabilized by side-chain interactions (Fitzpatrick et al., 2011; Eisenberg and Sawaya, 2017).

As a result, aggregation is concentration dependent, whereas folding is concentration independent. Thus, the lower the aggregation propensity of a protein, the higher concentration at which it can be safely expressed. Many proteins, we now know, have expression levels reaching or exceeding their critical concentration so that, in effect, the native state is a meta-stable conformation (Ciryam et al., 2015; Tartaglia et al., 2007). It is still unclear

why proteins live at the limit of or above their intrinsic solubility and why protein folding is, in fact, controlled kinetically rather than thermodynamically. To approach these questions, we need to have a better understanding of the structure-activity relationship between the amyloid and the globular state of proteins. Here we set out to explore the biophysical, structural, and evolutionary degrees of freedom that are available to thermodynamically favor globular structure with respect to the amyloid state.

We find that, rather than being simply associated by overlap of average biophysical properties, mutations in the globular and amyloid state are thermodynamically correlated. In addition, we show that the genetic code couples this correlation into a tight evolutionary relationship. We discuss the structural and evolutionary implications of this underestimated thermodynamic relationship. Finally, we speculate how this could have contributed to an amyloid origin of the globular protein universe.

RESULTS

Proteins with High Thermal Stability Are Enriched in Amyloid Sequences

It is well established that amyloidogenic segments (aggregation-prone regions [APRs]) are mostly located in buried positions in the native structure, but they can, to a lesser extent, also be found at exposed sites of functional importance, such as those required for binding or catalysis (Ganesan et al., 2016; Castillo and Ventura, 2009; Buck et al., 2013). Here we investigated the relationship between the aggregation propensity of amyloidogenic sequences and the free energy contribution of the same amino acid residues to the stability of the native state. To have a set of protein domains that is representative of the diversity of protein folds, we employed the SCOPe (structural classification of proteins–extended) database (release 2.06; Chandonia et al., 2017) and filtered for single-chain globular domains and 40% sequence identity using the CD-hit (cluster database at high identity with tolerance) algorithm (Fu et al., 2012). This yielded a dataset of 9,017 PDB structures of single-protein domains, amounting to 16,4791 residues in 23,329 amyloidogenic segments detected by the TANGO algorithm (Fernandez-Escamilla et al., 2004). The four main SCOP (structural classification of proteins) classes (α, β, α/β, and $\alpha+\beta$) are well sampled (Figure 1A, top panel) and contain similar amounts of sequences of pro- and eukaryotic origin (Figure 1A, bottom panel), showing that the set reflects a broad sample of protein sequence space. We first compared the APR frequency in the different SCOPe classes of globular protein folds, expressed as the number of APRs per 100 amino acids, and compared it with a set of intrinsically disordered proteins obtained from DisProt (Hatos et al., 2020; release 8.0.1, excluding ambiguous and obsolete regions, length larger than 25, resulting in 1,392 intrinsically disordered protein (IDP) regions from 1,039 proteins, amounting to 145,770 amino acid residues in total; Figure 1B). This showed that the frequency of APRs is very similar across SCOPe fold classes, although there is a slight increase in the topologically most complex α/β class, and it is only really reduced in intrinsically disordered proteins, confirming earlier observations (Linding et al., 2004). At the same time, the analysis revealed many outliers in the IDP category (i.e., IDPs containing APRs; Figure 1B), consistent with well-known aggregation-prone IDPs, including yeast prions and amyloid disease-associated human proteins (Chiti and Dobson, 2017). This basic observation already suggests that globular structure and aggregation propensity are associated properties. To probe this further, we focused on the globular SCOPe classes and calculated the thermodynamic contribution of APR residues to the stability of the native state, for which we employed the empirical force field FoldX, which computes local protein stability contributions per residue as part of its overall stability calculation (Schymkowitz et al., 2005), whereas the aggregation strength was determined using TANGO. We observed a clear association (Pearson's correlation coefficient = -0.27 ± 0.01, $p < 2.2e{-}16$) between the average contribution of an APR to the stability of its native structure and the aggregation strength of that same region (Figure 1C), again suggesting an association between globular protein structure and aggregation. To exclude that the presence of multiple APRs per domain would influence our analysis, we used TANGO to compare the intrinsic aggregation propensity of APRs in domains with a single APR with those containing more APRs (Figure 1D) and found no significant differences (Wilcoxon-Mann-Whitney test). Also, the observation that APRs tend to reside in buried positions (Figures 1E and 1F), where they contribute to the thermodynamic stability of the protein (Figure 1G), is even more pronounced in proteins that contain more than one APR. To address this further, we turned to a recent dataset on the proteome-wide determination of thermal protein stability in four species: *E. coli*, *T. thermophiles*, *S. cerevisiae*, and *H. sapiens* (HeLa cells) (Leuenberger et al., 2017). We filtered the raw data by LocTree3 subcellular localization prediction (Goldberg et al., 2014) to obtain melting temperature (Tm) values of 1,726 proteins with cytoplasmic or nuclear ("chromosomal" for bacteria) localization. For each species, we divided the proteins into two groups (Figures 1H–1O): one with proteins that have Tm values above the average for that species and the other with Tm values below the average (Table S1). We then calculated the sequence length normalized total TANGO score for each protein and compared the distribution of aggregation propensities in the high- and low-Tm groups (Figures 1H–1O). For the mesophilic HeLa cells (Figures 1H and 1I), *S. cerevisiae* (Figures 1J and 1K), and *E. coli* (Figures 1L and 1M), the amyloid-like aggregation propensity of proteins from the high-Tm group was significantly higher than of proteins from the low-Tm group. Interestingly, in the extremophile *T. thermophilus* (Figures 1N and 1O), which has an optimal growth temperature of about 65°C (Henne et al., 2004), the average length-normalized TANGO score of all proteins is equivalent to the high-Tm group in mesophilic organisms. No further increase in TANGO score was obtained by splitting the proteins of this extremophile into low-and high-Tm groups (Figure 1O), indicating that the hydrophobicity and the associated aggregation propensity are maximized in the entire proteome.

This analysis shows that within mesophilic species and between mesophiles and extremophiles, high thermal stability is associated with a high amyloid-like aggregation propensity, suggesting that protein stability and amyloid propensity are entangled properties.

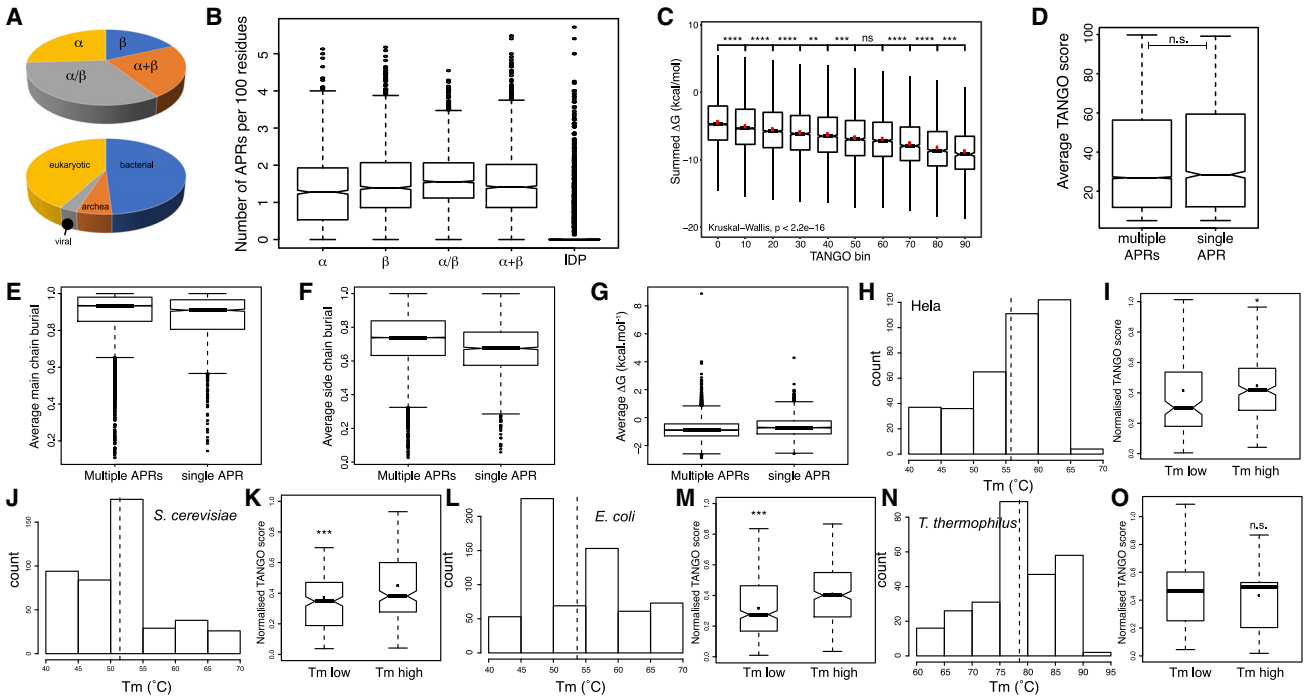

Figure 1. Stability and Aggregation Propensity Are Related

(A) Class and kingdom composition of the SCOPe dataset.

(B) Boxplot representation of the distribution of APRs in the SCOPe and IDP datasets.

(C) Boxplot showing the contribution of APRs to the stability of the native state calculated by FoldX in the SCOPe dataset in function of the predicted aggregation propensity by TANGO.

(D–G) Boxplots comparing APRs occurring in domains with one APR to those occurring in domains with more than one APR: the distribution TANGO score of APRs (D), the average main-chain burial (E), the average side-chain burial (F), and the average contribution of an APR to native-state stability (G, ΔG calculated by FoldX, in kilocalories per mole).

(H, J, L, and N) Histograms of the melting temperature (Tm) observed in whole-proteome protein stability measurements (Leuenberger et al., 2017) for HeLa cells (H), *S. cerevisiae* (J), *E. coli* (L), and *T. thermophilus* (N). The dotted line indicates the mean Tm of the proteome in question.

(I, K, M, and O) Boxplots comparing the normalized TANGO scores of proteins with a high or low Tm value in HeLa cells (I), *S. cerevisiae* (K), *E. coli* (M), and *T. thermophilus* (O).

The bottoms and tops of the boxes are the first and third quartiles, and the band inside the box represents the median; the dot indicates the mean. The whiskers encompass the minimum and maximum of the data. Significant differences were computed using a Wilcox rank test. Asterisks denote level of significance: n.s., not significant; *p < 0.05, **p < 0.01, ***p < 0.001.

The source files (Data S1) and R-scripts (Data S2) used to generate this figure are available.

Correlated Thermodynamic Response to Mutation between Tertiary Structure and the Amyloid State

To investigate the interdependence of protein stability and aggregation propensity in more detail, we compared the thermodynamic effect of point mutations in the native and amyloid conformation. Searching for proteins for which high-resolution crystallographic information was available for the globular native fold as well as for its amyloid state yielded a set of 11 amyloidogenic fragments derived from seven proteins (Figures 2A–2G): Bloom syndrome protein, transthyretin, insxulin, super oxide dismutase (SOD1), p53, β2-microglobulin, and lysozyme. We employed FoldX (Schymkowitz et al., 2005) to perform saturation mutagenesis (i.e., mutating each amino acid of the APRs to every other amino acid in the native and the amyloid structure) and calculated the associated change in free energy (ΔΔG values in kilocalories per mole) of both structures. The heatmap summarizing these 1.368 mutations (Figure 2H) clearly shows that the effects of mutation on the stability of native and amyloid structures are correlated (correlation coefficient = 0.46, p < 2.2e–16, Pearson's product moment correlation test), in line with amyloid and globular structure being associated properties. It is also clear from Figure 2H that there are outliers; i.e., the regions of the plot corresponding to mutations that destabilize the amyloid state without overly perturbing the native state. However, even when considering liberal thresholds for tolerated native-state destabilization (<1.0 kcal/mol), only 53 of 1.368 mutations or 3.87% significantly destabilize the amyloid (>1.5 kcal/mol; i.e., the equivalent of loss of one backbone-backbone hydrogen bond; indicated by the green box in Figure 2H). Thus, the number of mutations that destabilize the amyloid state without simultaneously disrupting the structure of its conjugate native tertiary protein is inherently restricted by the context of globular protein structure. Strikingly, when we considered the DNA sequences of the corresponding genes of the proteins under study, we found

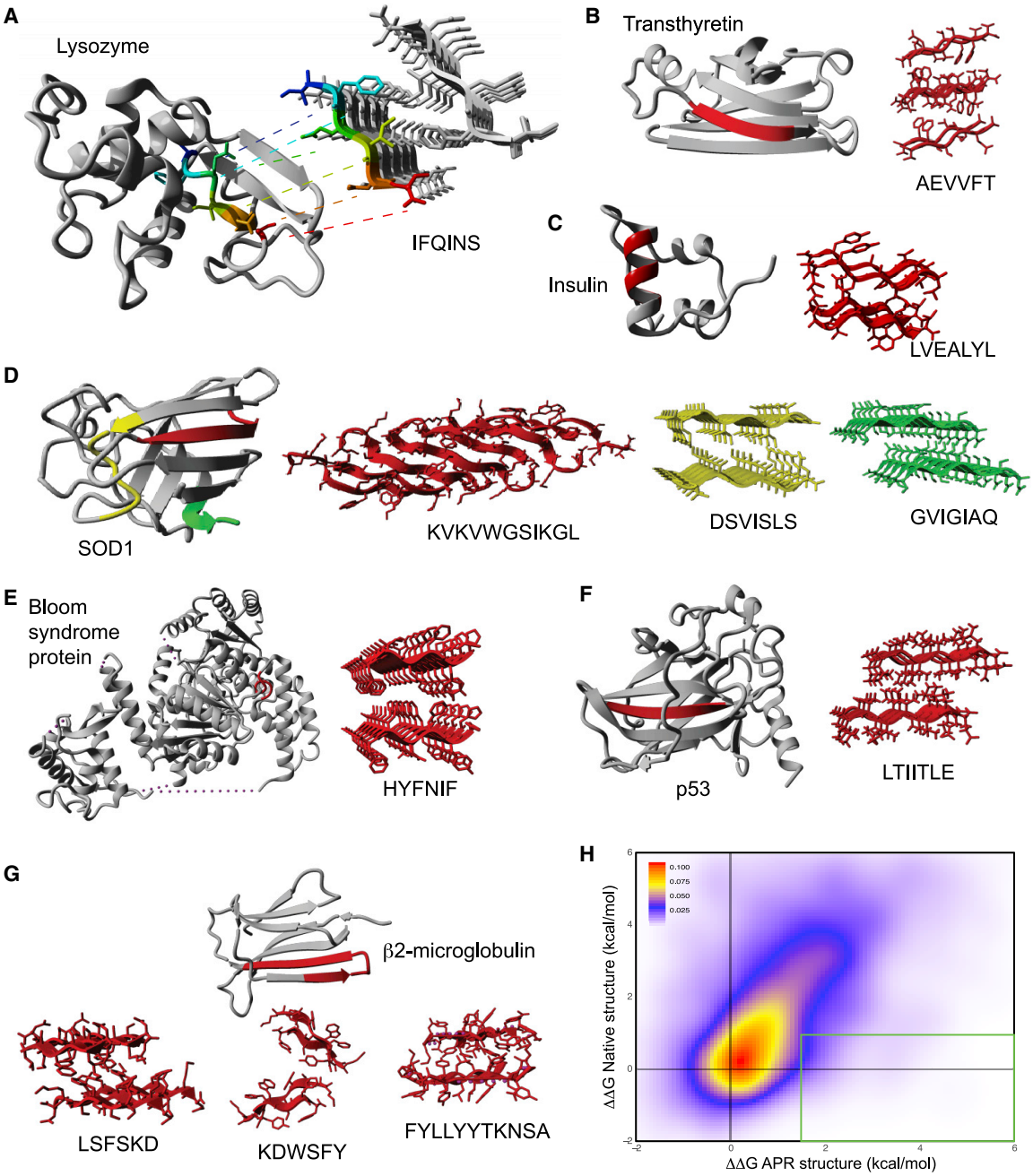

Figure 2. Mutational Energies of APRs and Native Structures Are Coupled

(A–G) Schematic representations of the crystal structures of APRs and their cognate native states for lysozyme (A), transthyretin (B), insulin (C), SOD1 (D), Bloom syndrome protein (E), p53 (F), and β2-microglobulin (G). The APR segment is highlighted in color in an otherwise gray native-state structure. The PDB identifiers used are listed in STAR Methods.

(H) Density plot of the free energy change in thermodynamic stability (ΔΔG, FoldX, in kilocalories per mole) associated with mutation in the native state versus the APR state. The green box encompasses the APR-destabilizing mutations (ΔΔG at least 1.5 kcal/mol) that may be tolerated at the native structure level at a cutoff of ΔΔG no larger than 1 kcal/mol. The source files (Data S1) and R-script (Data S2) used to generate this panel are available.

that, of these 53 mutations, only 15 or 1.10% of all mutations are accessible by a single-base-pair substitution. This suggests that codon usage further enforces the coupling of these thermodynamically correlated structural conformations.

Thermodynamic Coupling between the Native and Amyloid State by the Genetic Code

To understand the mechanisms and degree of coupling between the native and amyloid state by codon usage, we analyzed the

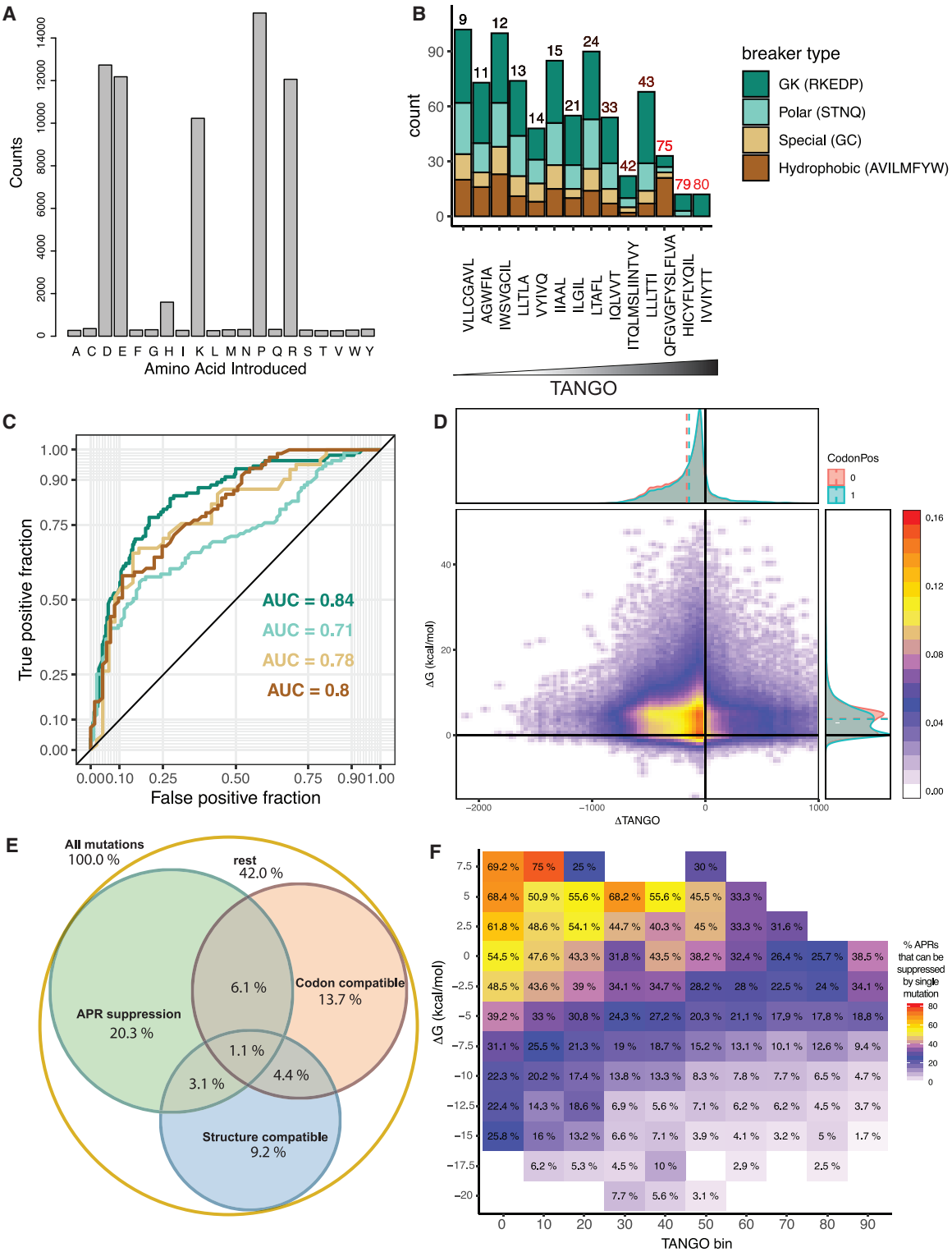

Figure 3. Codon Usage and Native-State Stability Reduce the Number of Possible Aggregation-Suppressing Mutations in a Systematic Mutation Scan of the SCOPe Set of Protein Structures

(A) Mutational screen for mutations that completely suppress an APR (TANGO score of mutant = 0) for all APRs with a TANGO score of more than 50 in the SCOPe set. The height of the bars indicates the number of times each amino acid is found in the suppressed mutant.

(legend continued on next page)

conservation of both properties by computationally comparing the ability to suppress amyloid propensity by single amino acid mutations in a large variety of protein folds. To do this, we set out to mutate, *in silico*, each amino acid in each APR in the SCOPe set described above to glutamate, aspartate, lysine, proline, and arginine. These amino acids have been shown previously to have the strongest aggregation-reducing effects of amino acid substitutions and are collectively called gatekeepers (GKs) (Ganesan et al., 2016; Rousseau et al., 2006; van der Kant et al., 2017; Van Durme et al., 2016). To further illustrate this aspect here, we performed an exhaustive mutation scan of the SCOP dataset, selected those that fully suppress (reduce to zero) an APR with an average TANGO score above 50 (to restrict the analysis to the strongest regions) and analyzed the type of substitutions this involved. These data confirm that mutation to P, R, K, D, and E is required to suppress the stronger APRs, allowing us to restrict our *in silico* mutation screening to these residues (Figure 3A). Then we reanalyzed a published dataset of deep mutational scanning of 10 different proteins, where each mutation was annotated with a normalized fitness score in a recent meta-analysis (Gray et al., 2017). First, we calculated which mutations would fully suppress the intrinsic aggregation propensity of each of the APRs in this dataset, taking only the TANGO score into account and ignoring the structural or codon context (Figure 3B). This showed again that, for stronger APRs, mutations to GK residues are the only effective option, whereas for weaker APRs, other options are possible. Next, we used a receiver operating characteristic (ROC) curve analysis to assess how well FoldX ΔΔG values could predict the fitness outcome (tolerated or disruptive) of each suppressing mutation (Figure 3C). In this analysis, a mutation was classified as tolerated when their normalized fitness effect was reported to be above 0.8. In a ROC curve, the fraction of correct binary classifications (tolerated or disruptive) at each threshold of the predictor (FoldX) is plotted against the fraction of false classifications. The area under the curve gives an indication of the performance of the predictor, in this case FoldX, at the classification problem, in this case classifying mutations into tolerated or disruptive. This showed (Figure 3C) that FoldX performance is overall good at this task but is best in the case of GK residues. Given these results and the fact that, for the current analysis, we were mostly interested in high-scoring, conserved APRs, we restricted subsequent *in silico* screens for APR-suppressing mutations to P, R, K, D, and E. For each mutation, we evaluated its effect on native-state stability using FoldX and its effect on aggregation propensity using TANGO. In addition, we mapped the residues back to their corresponding codons in the gene sequence to evaluate effects from codon usage bias. We restricted the dataset to APRs that had a length of at least five amino acid residues and an average TANGO score equal to or larger than 5.0% and classified each amino acid change by accessibility with a single DNA mutation (Figure 3D). Ultimately, this yielded a dataset of 821,420 mutations to the GK residues D, E, K, R, or P in 23,263 APRs (totaling 164,284 amino acid positions) derived from 7,876 domains. Of all mutations, 30.7% significantly suppressed aggregation strength (TANGO < 5%), 25.4% were codon accessible, and 17.8% did not disrupt the native structure (ΔΔG < 0.5 kcal/mol) (Figure 3D). Cross-sectioning these three requirements of the restrictions imposed by codon usage and the structural context leaves only 1.1% of mutations that can suppress aggregation using codon-allowed single-base mutations without compromising the native structure compared to 4.2% when also considering artificial mutations to any of the GKs (Figure 3E). Of the five GK residues, arginine is easiest to place, and the four others appear with approximately half of its frequency in the group of the possible mutations (Figure S1). Thus, on a mutation-per-residue basis, it is apparent that codon usage further strengthens the thermodynamic correlation between the amyloid and native state.

Because each amyloidogenic segment can potentially be altered by many single mutations, we can also estimate the quantity of amyloidogenic segments that can be fully suppressed by codon-allowed and structurally conservative GK mutations. Plotting the percentage of suppressible segments per native stability bin, we can see that, although globally approximately one-fourth (24.5%) of all APRs can, in principle, be suppressed by single-nucleotide mutations, the majority of these consist of APRs with low aggregation propensity in regions that also have a low contribution to the stability of the native structure (Figure 3F). It is, however, much more difficult to uncouple both properties when the thermodynamic stability of both states is high (Figure 3F). It is therefore to be expected that sequences that are strongly coupled by high amyloid propensity and high native-state stability are also strongly conserved.

To illustrate this further, we created a network of the transitions that can occur between amino acids, based on single-base-pair substitutions and codon usage, the basic evolutionary operator. The substitution frequency between amino acids is indicated by colored lines (Figure S2; red and yellow are frequent

(B) Types of suppressing mutations in the deep mutational scanning dataset. Bars depict the number of mutations predicted to be suppressing to the APRs identified in the dataset. Colors indicate amino acid type, and APRs are ordered along the x axis according to their TANGO score.
(C) Receiver operating characteristic (ROC) curve for the prediction of the fitness outcome of a mutation (with a fitness score of more than 0.8 corresponding to a tolerated mutation) from the ΔΔG calculated through FoldX. ROC curves were produced for each amino acid type (color-coded as in B), and area under the curve (AUC) is reported for each prediction.
(D) Density plot of the change of free energy of the native state (ΔΔG, FoldX, in kilocalories per mole) upon mutation versus the associated change in predicted aggregation propensity (TANGO). The top and right insets show histogram projections of the same data, split by whether (CodonPos = 1) or not (CodonPos = 0) the mutations are accessible through single-base changes in the cognate genes. The segmented lines indicate the means of the respected groups.
(E) Venn diagram grouping the mutations from (A) into three groups: APR suppression (TANGO reduced to 0 by the mutation), codon compatible (mutation accessible through a single-base change of the cognate gene), and structure compatible (mutations with a ΔΔG value [FoldX] of less than 0.5 kcal/mol).
(F) Heatmap of the percentage of APRs for which suppressing mutations can be identified in function of the contribution to the native-state stability of the APRs (ΔΔG, FoldX, in kilocalories per mole) and its aggregation propensity (TANGO).
The source files (Data S1) and R-scripts (Data S2) used to generate this figure are available.

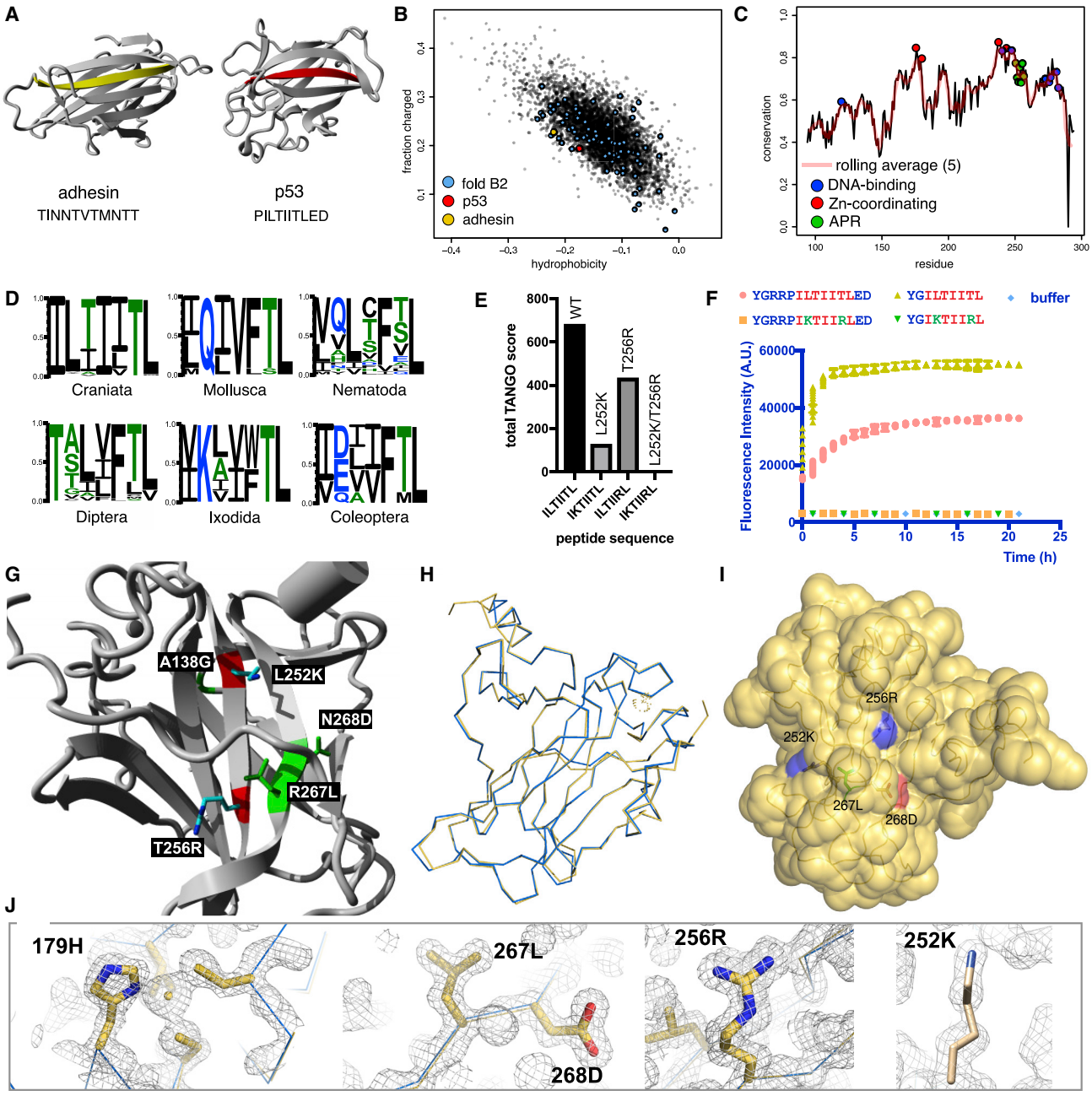

Figure 4. Evolutionary and Protein Engineering Analysis of an APR in the p53DBD

(A) Structures of the APR-free adhesin fold (PDB: 1R17) and of the p53-family fold (PDB: 2AC0) with the APR highlighted red and the equivalent strand in the adhesin highlighted yellow.

(B) Fraction of charged amino acids and hydrophobicity for the entire fold class B in dataset 1, with fold class B2 members highlighted blue, human p53 red, and bacterial adhesin yellow.

(C) Degree of sequence conservation of the p53 DNA-binding domain (DBD) in all craniates per residue (black line) and as a rolling average per five residues (red). Functional residues are marked in blue (DNA-binding) and red (Zn ion coordination), and APR residues are marked in green.

(D) APR sequence logos for several phylogenetic groups in dataset 5.

(E) Total TANGO score of the ILTIITL sequence and selected mutants.

(F) Aggregation kinetics of the indicated peptides monitored by Thioflavin-T fluorescence.

(G) Location of selected mutations in the native structure of p53DBD.

(legend continued on next page)

substitutions, and blue is rare.). When functional protein evolution is considered, the amino acids are grouped into hydrophobic (HP), polar (PO), and charged (+/−). Single-base-pair changes favor a conservation of class, which has been noted before and is generally rationalized to favor mutations that retain biological function by replacing like with like but also allows a low frequency of changes between classes, allowing evolutionary changes. When this scheme is considered from the point of view of amyloid-like aggregation, the amino acids can be grouped very similarly into APR, neutral (NT), or aggregation GK. This side of the plot clearly shows that codon bias also tends to conserve amyloid-like propensity along with biological function, including globular structure.

Amyloid Addiction of the p53 Core Domain Fold

To understand the consequences of codon-enforced thermodynamic entanglement of native and amyloid-like interactions during protein evolution, we took a closer look at fold b.2 ("common fold of diphtheria toxin/transcription factors/cytochrome f") of the SCOPe database, which contains the superfamily b.2.5 ("p53-like transcription factors"). For p53 itself, we previously identified a very-high-scoring amyloidogenic segment in its HP core (Xu et al., 2011) that was later confirmed by others (Soragni et al., 2016; Wang and Fersht, 2017; Das and Makarov, 2016; Figure 4A, red), although it has been also shown that the protein, in addition, can undergo phase separation (Boija et al., 2018) and amorphous aggregation (Wang and Fersht, 2017). The b.2 fold has 75 unique PDB entries (corresponding to 78 unique sequences) in the SCOPe set, two of which do not have an amyloid-prone sequence according to TANGO (at a threshold of 1.0%): Invasin AfaD of *Escherichia coli* and adhesin SdrG of *Staphylococcus epidermidis*, both in superfamily b.2.3. Figure 4A shows the structures of adhesin SdrG (PDB: 1R17; amino acids 425–582) and human p53 (PDB: 2AC0; a monomer with the DNA-binding α helix removed; amino acids 106–275), with the β strand containing the prototypical APR sequence P**ILTIITL**ED of p53 colored red and the APR-free corresponding strand in the adhesin colored yellow (the residues constituting the core of the APR are in bold font, the flanking GK residues are in normal font). Structural alignment (utilizing MUSTANG; Konagurthu et al., 2006) of the two superfamilies has a root-mean-square deviation (RMSD) of 1.815 Å over 45 aligned residues with just 2.22% sequence identity. Both folds are close together at an edge position in a plot of the fraction of charged amino acids over total hydrophobicity (Figure 4B), showing that their overall amino acid composition is very similar. None of the 20 proteins in the SCOPe set of the p53-like superfamily b.2.5 is APR free, according to the TANGO algorithm, suggesting that the aggregation propensity of the p53 APR **ILTIITL** (or equivalent) is an exquisitely conserved feature in this superfamily.

To analyze this in more detail, we wanted to find out whether p53 homologs without the ILTIITL amyloid can be identified altogether. To this end, we performed a HMMER (Prakash et al., 2017) search of UniProtKB with the p53DBD (DNA-binding domain). At an E-value of <0.03 for hits, this yielded 1,278 sequences. We filtered this set at 95% sequence identity, and to ensure that we only compared *bona fide* homologous structures, we removed sequences missing the entire amyloid-containing segment as well as those that lacked more than one equivalent of the zinc-ion-coordinating residues C176, H179, C238, and C242 of the (human) p53DBD. Of the final 337 proteins (dataset 5), we find that only six have a TANGO score of less than 1.0% in the equivalent of the ILTIITL stretch, whereas another 10 score between 1.0% and 5.0% (Table S2). Of the six, the closest divergence time from humans is about 800 million years ago (Ma), and of the 10, about 700 Ma (www.timetree.org; Kumar et al., 2017). The identity with the human p53DBD ranges between 27% and 40%. We find that the ILTIITL sequence is highly conserved throughout nearly the entire subphylum Craniata (average TANGO score, 76 ± 13 in 136 members; Table S3), which, in dataset 5, covers an evolutionary distance to humans of 615 Ma at an average sequence identity of 66%. Of all amino acids in the DBD, the amyloidogenic residues are among the most highly conserved (Figure 4C). At increasing evolutionary distance to craniates, the sequence diversity of that segment generally increases, and along with it, the TANGO score standard deviation for members of a clade (Table S3; Figure 4D).

The ILTIITL segment thus appears to be an integral part of the p53 family DBD structure. p53-like folds with weaker variants of it, or even entirely lacking this sequence stretch, can only be found at very long evolutionary distances. On the other hand, the evolutionarily unrelated instances of the p53-like fold that lack this segment altogether show that it is not required to generate a functional instance of this fold. Thus it appears that the amyloidogenicity of this segment is in an evolutionary culde-sac; by its strong contribution to the stability of the native state, its amyloidogenic propensity was also conserved over long evolutionary distances.

Suppressing a 600-Ma-Old APR Requires Multiple Concomitant Aggregation-Inhibiting and Compensatory Stabilizing Mutations

To validate that the coupling between the stability of the amyloid and native states is evolutionarily enforced, we investigated whether it is possible to uncouple amyloid aggregation and native-state stability using protein engineering. Given that the p53 fold is possible without the ILTIITL sequence, we wondered how many mutational steps it would take to eliminate the aggregation propensity of the ILTIITL segment from the p53 sequence itself: is this feasible by small steps, or does it require evolutionary improbable alterations? We calculated the predicted energy changes based on the DNA-bound tetrameric structure (PDB: 2AC0; Kitayner et al., 2006) using FoldX. Given its high average TANGO score (89%), strong contribution to native-state

(H) Backbone alignment of the crystal structures of p53cc (gold) and the WT (blue).
(I) Surface rendering of the crystal structure of p53cc with the introduced side chains highlighted. A blue surface marks a positive charge and a red surface a negative charge.
(J) Electron density maps (contoured to 1σ) around the zinc binding site (H179) and mutated residues in p53cc.

stability (i.e., low summed free energy contribution according to FoldX, $\Delta G_{sum} = -12.4$ kcal/mol), and very strong evolutionary conservation, the p53DBD APR represents a case of high amyloid-native state coupling that appears difficult to suppress by codon- and structure-compatible mutations. Indeed, there is not a single mutation to a GK residue that is predicted to be compatible with the thermodynamic stability of the native state ($\Delta\Delta G$ of < 0.5 kcal/mol). Of the two least destabilizing aggregation-reducing mutations (T256R and L252K; Figure 4E; Table S4), only the less effective one (T256R) is accessible by a single base change, whereas L252K would require changing all three bases. Moreover, each mutation is predicted by FoldX to still significantly destabilize the folded p53DBD domain (2AC0) by an extent that has been shown previously to lead to misfolding and aggregation of the protein (De Smet et al., 2017; Xu et al., 2011) ($\Delta\Delta G$ T256R = 1.88 kcal/mol and $\Delta\Delta G$ L252K = 1.24 kcal/mol per monomeric unit). Hence, neither mutation is likely to be selected during the course of evolution, and moreover, TANGO suggests that the combination of both is required to completely suppress aggregation of this APR (Figure 4E). We corroborated experimentally that the aggregation kinetics of the double mutant version of the ILTIITL peptide were indeed suppressed (Figure 4F), both with and without the natural sequence context of the peptide.

To introduce both mutations while maintaining the native state of the protein, the $\Delta\Delta G$ analysis above showed that, for each aggregation-reducing mutation, at least one concomitant compensatory mutation would need to be found to rescue the thermodynamic stability of the native p53DBD. A FoldX scan for compensatory mutations identified R267L and N268D on the adjacent β strand and A138G in a distal loop. So to completely suppress aggregation while maintaining protein structure and DNA binding, we had to introduce two aggregation-suppressing mutations (L252K/T256R) and three compensating stabilizing mutations (A138G, R267L, and N268D) (Figure 4G). We dubbed the final quintuple mutant (A138G/L252K/T256R/R267L/N268D) "p53 charged core" or p53cc. The need for combining two aggregation-breaking residues with three compensatory stabilizing mutations again illustrates the high degree of coupling between both properties and makes it highly unlikely for natural variation to eliminate the amyloid propensity of this segment; this would require four concomitant single-base substitutions to suppress the amyloid propensity together with three additional single-base substitutions to maintain a stable native fold.

To verify the structural integrity of p53cc, we expressed the p53DBD (residues 89–311) containing the five-amino-acid-residue mutations in bacteria and purified and crystallized the protein. We collected data from a single crystal that diffracted to 1.63 Å. The structure was solved by molecular replacement using the p53 wild-type (WT) DBD structure already deposited in the PDB as a search model (accession code of the search model, PDB: 2XWR; chain A, resulting structure, PDB: 6SL6; Table S5). The backbone alignment of p53WT and p53cc has an RMSD of 0.49 Å over 199 aligned residues (Figure 4H). We find all mutations to be well resolved and placed without energetic clashes (Figures 4I and 4J). The structures of other central features of the p53DBD, such as the zinc ion and its coordinating residues, are virtually identical to the WT. Importantly, as predicted by FoldX, the charges at the end of the long side chains of arginine and lysine that we placed in the APR in the core of the DBD reach the surface of the structure (Figure 4I). When we measured the thermal stability of the WT and mutant p53, we observed a lower Tm value for the mutant (Figure 5A; Tm = 37.7°C ± 0.55°C) than the WT (Figure 5B; Tm = 42.4°C ± 0.50°C) (Figure 5C). To assess the functional integrity of the mutant p53, we first measured the DNA-binding activity of the purified DBD by two orthogonal methods using fluorescently labeled DNA oligonucleotides: microscale thermophoresis (MST; Figure S3) and fluorescence anisotropy (FA; Figure 5D). Both methods are in general agreement and show that the affinity of the mutant for an oligo containing the consensus p53 DNA-binding motif is the same as the WT (mutant K_D = 1.28 μM ± 0.28 μM; WT K_D = 1.23 μM ± 0.20 μM in FA). To test the ability of p53 to engage with its target promoters in a natural context, which requires more complex steps than just DNA binding and, hence, tests the mutant in a more complex biological function, we transfected full-length WT or p53cc into the p53-negative human cell line Saos-2 (Sarcoma Osteogenic-2) and measured promoter activation for seven different genes by qPCR (Figure 5E). Across the seven promoters, p53cc had an average activity of 0.95 compared with the WT protein, a difference that was not statistically significant, although individual genes showed some differences. In summary, these results demonstrate that we did not disrupt protein structure and function by reducing amyloid propensity.

We determined the aggregation kinetics of WT and mutant DBD using the amyloid-specific dye pentameric formyl thiophene acetic acid (p-FTAA; Figure 5C) and 8-anilinonaphthalene-1-sulfonic acid (ANS; Figure 5F), a dye that shows increased fluorescence upon binding to exposed HP patches. The dye binding kinetics for p-FTAA and ANS show a similar decrease in the aggregation kinetics for the mutant compared with the WT protein (Figures 5F and 5G). Moreover, according to transmission electron microscopy performed at the end of the kinetics studies, the aggregates formed by WT DBD are larger, and fibrillar structures can be observed (Figure 5H), whereas for mutant DBD, only smaller, spherical structures were seen (Figure 5I), suggesting non-amyloid aggregation or phase separation. Taken together, these data show that a small number of mutations is sufficient to eliminate an important amyloidogenic segment from the p53 structure without disrupting DNA binding and transcriptional activation. Moreover, the case shows that such mutations can be detected with reasonable accuracy using our computational approach. However, our data also illustrate why a buried APR is an evolutionary cul-de-sac; to reach this combination of mutations by natural variation would involve intermediate sequences that would be severely functionally impaired. In addition, one of the crucial mutations (L252K) requires changing all three bases of the codon at once, making an evolutionary path toward this solution extremely improbable.

Generalization: Topological Invariance of Amyloid Addiction

To investigate whether the results obtained with p53 are representative of many globular folds, we investigated, in the SCOPe set, the difference between APRs that can be fully suppressed

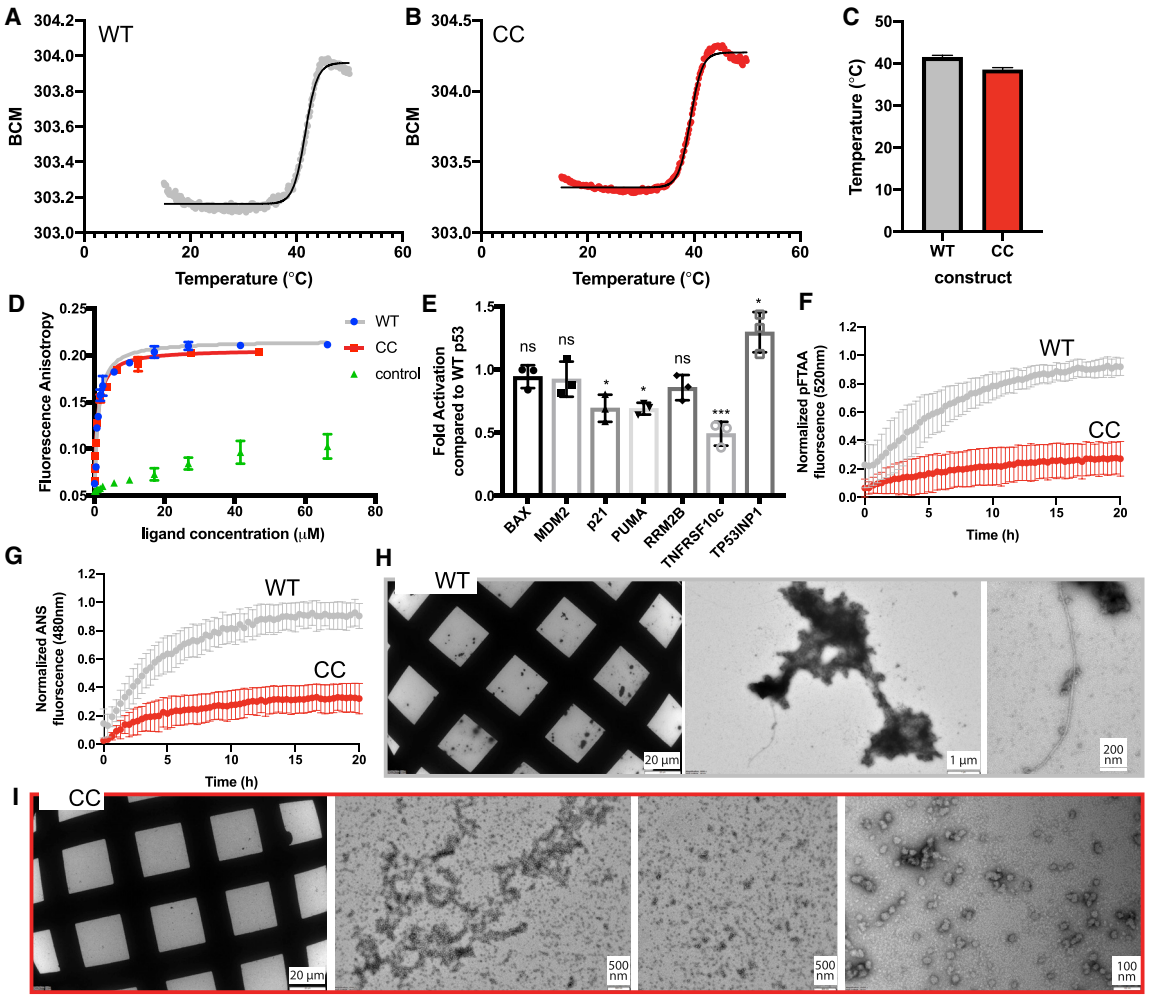

Figure 5. Biophysical Analysis of p53cc

(A) Heat denaturation of WT p53DBD, monitored by intrinsic fluorescence plotted as the barycentric mean (BCM) of the emission spectrum. The black line indicates the fit performed to determine the midpoint of the transition.

(B) Same as (A) but for the CC mutant.

(C) Average Tm values obtained from five biological replicate measurements.

(D) DNA-binding affinity of p53cc and the WT, measured by FA. Error bars indicate standard deviation of five biological replicates, each measured in three technical replicates.

(E) Degree of promoter activation of p53cc relative to WT p53 in Saos-2 cells, measured by qPCR. Error bars indicate standard deviation of three biological replicates, each measured in three technical replicates.

(F) Aggregation kinetics of p53cc and the WT, measured by p-FTAA fluorescence.

(G) Aggregation kinetics of p53cc and the WT, measured by ANS fluorescence.

(F and G) Error bars indicate standard deviation of five biological replicates, each measured in three technical replicates.

(H) Transmission electron microscopy (TEM) analysis of aggregates of WT p53.

(I) TEM analysis of p53cc.

(H and I) Representative images from three biological replicates.

(TANGO reduced to zero) by a single, codon-compatible, and structure-compatible (FoldX ΔΔG < 0.5 kcal/mol) mutation (called rescuable) versus those that cannot (called non-rescuable). First of all, we found a similar frequency of non-rescuable APRs in each of the four main SCOP classes (Figure 6A) and also found no apparent bias toward any specific secondary structure element of the segment in the native state (Figure 6B). This is in agreement with earlier observations that APRs occur in all elements of secondary structure despite the fact that the segment will adopt a β sheet conformation in the aggregated state (Rousseau et al., 2006; Linding et al., 2004). Because we already showed that intrinsic aggregation propensity, codon usage, and the native state structural context are strong determinants of how easily an APR can be suppressed (Figure 3C), we used these parameters to take a closer look at three cases from the main SCOP classes other than the one to which p53DBD

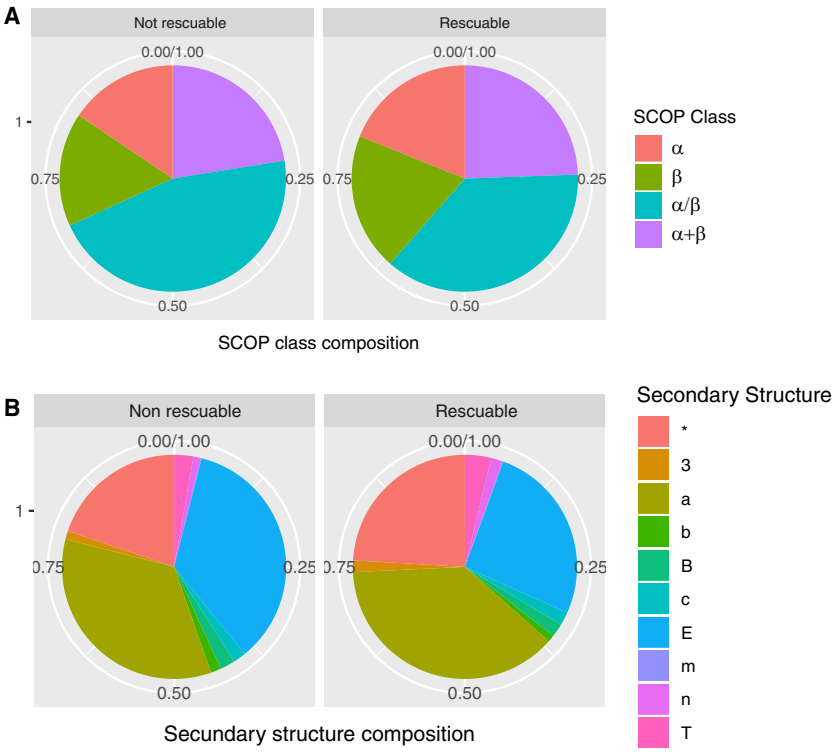

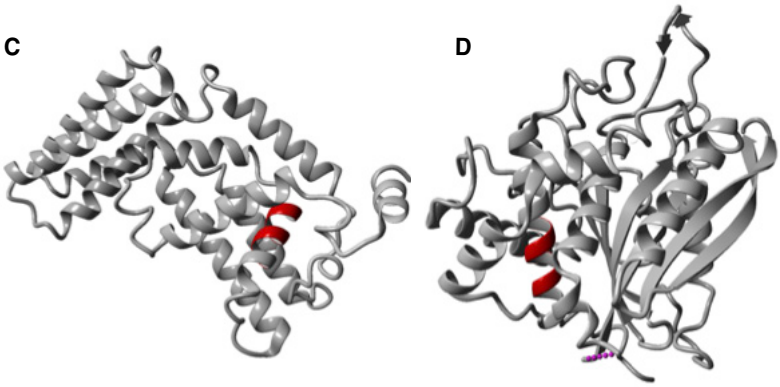

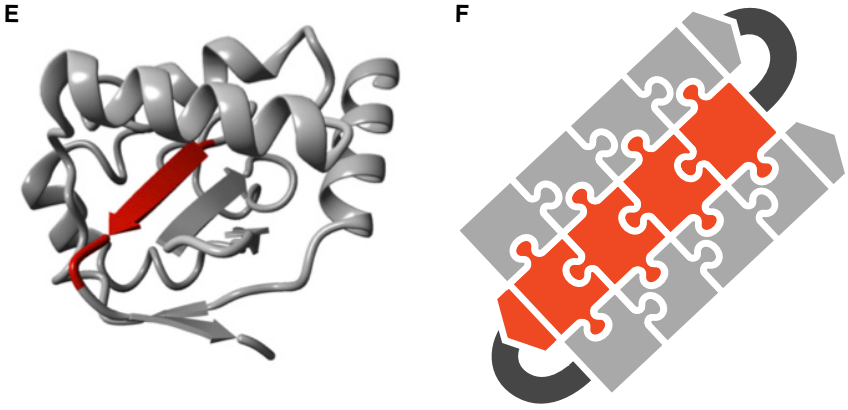

Figure 6. Topological Invariance of Amyloid Addiction

(A and B) Comparison of APRs that can be fully suppressed by a single codon-compatible mutation (rescuable) with those that cannot, in terms of SCOP class (A) and secondary structure element (B) in which they occur, following the FoldX code for secondary structure annotation (*, unclassified; 3, 3-10 helix; a, α helix; b, parallel beta conformation; B, antiparallel beta conformation; E, β strand; c, random coil; m, helix C-cap; n, helix N-cap; T, turn).

(C) Example of a conserved APR in an all-α fold (SCOP class a): the VPS9 domain of Rab5 (*Homo sapiens*; PDB: 1TXU).

(D) Example of a conserved APR in the α/β fold (SCOP class c): glutaminyl-peptide cyclotransferase (*Homo sapiens*; PDB: 2AFW).

(E) Example of a conserved APR in an α+β fold (SCOP class d): E3 ubiquitin-protein ligase NRDP1 (*Homo sapiens*; PDB: 2FZP).

(F) Schematic representation illustrating the APR addiction principle.

The source files (Data S1) and R-scripts (Data S2) used to generate this figure are available.

belongs (b). To this end we searched the SCOP set for human domains with an APR with a high TANGO score (>80%), a high average side-chain burial (>0.8), and a minimum length of 7 amino acids that have no mutation that reduces the TANGO score to zero with a predicted ΔΔG below 1.5 kcal/mol. In the all-α-helical folds (class a), we identified the VPS9 domain of the Rab5 guanosine diphosphate (GDP)/guanosine triphosphate (GTP) exchange factor (Figure 6C). This contains an α-helical stretch with the sequence TLIYIVL that has a TANGO score of 86.5 per residue and an average side-chain burial of 0.91 in the native state and contributes – 13.1 kcal/mol to native state stability. A HMMER search for homologs with an E-value cutoff, followed by redundancy filtering at 95% (CD-hit), left 2,302 unique sequences. Of these, only 8 had a TANGO score below 1, with a closest divergence time of 600 Ma to humans. In the α/β class (c), which is generally regarded as the topologically most complex class that is enriched in obligate chaperone clients (Kerner et al., 2005), we further looked at glutaminyl-peptide cyclotransferase (Figure 6D), which contains an APR with the sequence ILQVFVL, a native helical conformation and an average TANGO score of 95.2% per residue, an average side-chain burial of 0.93 in the native state, and a contribution to its thermodynamic stability of −14.4 kcal/mol. HMMER searching with redundancy filtering yielded 1,285 homologous sequences, 117 of which have a TANGO score below 1, of which the closest evolutionary distance to human was 800 Ma. Finally, in the α+β fold class, we investigated the E3 ubiquitin protein ligase NRDP1 (Figure 6E). This contains an APR with a native β strand conformation and the sequence LVMIFA, with a TANGO score of 85.5% per residue, a side-chain burial in the native state of 0.84, and a contribution to its stability of −9.91 kcal/mol. HMMER searching followed by redundancy filtering identified 109 homologous sequences, of which only one had a TANGO score below 1, corresponding to an evolutionary distance of 800 Ma.

Taken together, these cases and the wider studies shown in Figures 6A and 6B clearly show that the evolutionary and thermodynamic profile of the APR studied in the p53 cases is not an exception, and a general picture emerges that regions with a high aggregation propensity and a high contribution to native state stability show high evolutionary conservation (Figure 6F).

DISCUSSION

Here, we find that cognate globular and amyloid structures possess correlated thermodynamic responses toward mutation, which is in line with earlier results obtained by Lee et al. (2010) that translationally optimal codons associate with APRs. In addition, we find that the genetic code couples this thermodynamic correlation into an evolutionary relationship. These findings entail several structural and evolutionary implications. First, they suggest that the observed association between protein stability and protein aggregation is not a mere side effect of similar average biophysical properties (hydrophobicity, β strand propensity, charge) but is determined by fundamental and highly sequence-dependent structural similarities between both conformations. This explains why only a minority of mutations in a protein can lower amyloid-like propensity without affecting stability (Ganesan et al., 2016). Second, the restrictions on amino acid substitutions by the genetic code further tighten this relationship by favoring mutations that conserve both structural properties. Accordingly, we find that the amyloidogenicity of segments that are strong contributors to protein stability are also strongly conserved and cannot be uncoupled by single-base substitutions. Third, this means that evolutionary pressure toward increased protein stability will also increase the amyloid-like propensity of proteins, and we find here that thermostable proteins in mesophiles and the entire proteome of thermophiles are indeed more amyloidogenic. Fourth, more stable proteins will therefore be less efficient at folding because of kinetic competition with aggregation. As a result, allowing selection of stable protein variants will require the support of mechanisms for kinetic compartmentalization between folding and aggregation, including aggregation GKs (De Baets et al., 2014; Reumers et al., 2009; Rousseau et al., 2006; Monsellier and Chiti, 2007) and chaperones (Ramakrishnan et al., 2020; Scior et al., 2016). In agreement, it has been shown recently that inhibition of Hsp90 function results in selection of polio virus variants with reduced aggregation but at the expense of protein stability (Geller et al., 2018). This suggests Hsp90 indeed supports the selection of stabilizing protein mutations by managing their correlated aggregation propensity. Finally, from all of the above, we speculate that amyloid propensity could have been a driver for the evolution of globular protein structure by reciprocal selective enrichment.

Indeed, the hypothesis for an amyloid-driven origin of life has been posited recently by several groups (Dale, 2006; Maury, 2009; Greenwald and Riek, 2012). Amyloid peptides possess many of the properties that would make them stronger candidates than RNA for being the first self-replicating and catalytic molecules of life. Small amyloidogenic peptides can be spontaneously generated by organic chemical reactions under conditions prevailing on prebiotic earth (Miller, 1953; Parker et al., 2014; Bada, 2013). Amyloids can condensate under such harsh conditions (Greenwald et al., 2016), conformationally perpetuating their sequence information in a selective manner (Maury, 2015), but also allow variation and divergent evolution (Wickner et al., 2009). Additionally, it has been demonstrated recently that amyloid fibrils can catalyze peptide bond condensation in a templated manner (Rout et al., 2018). From a functional perspective, amyloid assembly can provide catalytic surfaces that further promote their proliferation (Cohen et al., 2013) as well as diverse enzymatic activities (Tena-Solsona et al., 2016; Omosun et al., 2017; Al-Garawi et al., 2017; Ivnitski et al., 2014). Their mode of assembly can also provide binding interfaces stabilizing nucleic acid interactions and vice versa (Braun et al., 2011; Macedo and Cordeiro, 2017). Amyloid assembly can mediate compartmentalization and membrane formation (Boke et al., 2016; Mahalka et al., 2011; Domanov and Kinnunen, 2008). Finally, nature still exploits the amyloid conformation for functional purposes (Fowler et al., 2007; Otzen and Riek, 2019). It has therefore been proposed that the amyloid state is a "common ancestor" fold from which the globular protein universe could have emerged (Greenwald and Riek, 2012; Maury, 2009), but a proximate structural mechanism that could drive the transition from linear amyloid peptides to globular protein-like structures has not yet been identified. Our current findings

suggest that the intrinsic structural properties of amyloid and globular structure possess similar thermodynamic proclivities that could easily provide the gradient for their co-evolutionary selection. Amyloid toxic gain of function in human disease is believed to be largely exerted by meta-stable soluble amyloid-like oligomers (Breydo and Uversky, 2015; Chiti and Dobson, 2017; Benilova et al., 2012). The globular-like structure of these oligomers (Laganowsky et al., 2012) suggests that the same mechanism leading to amyloid toxicity in human disease could have served the emergence of globular structure. A large fraction of proteins supersaturated under physiological conditions (Ciryam et al., 2015; Tartaglia et al., 2007) could be a relic of this process, along with the requirement of tight protein quality control and the devastating effect of the loss thereof with aging (Hipp et al., 2019; Labbadia and Morimoto, 2015).

STAR★METHODS

Detailed methods are provided in the online version of this paper and include the following:

- KEY RESOURCES TABLE
- LEAD CONTACT AND MATERIALS AVAILABILITY
- EXPERIMENTAL MODEL AND SUBJECT DETAILS
  - Cell culture
- METHOD DETAILS
  - Transfection
  - Cloning and mutation of p53 DBD
  - Protein expression and purification
  - Crystallization and structure determination
  - Dynamic light scattering
  - ThT and pFTAA binding
  - Fluorescence anisotropy
  - Microscale thermophoresis
  - Quantitative PCR
- QUANTIFICATION AND STATISTICAL ANALYSIS
  - SCOPe analysis and artificial protein datasets
  - Evolutionary analysis of p53
  - PDB entries of APRs and corresponding full-length protein structures
  - Deep mutational scanning analysis for suppressing mutations
  - Codon usage correlation analysis
  - Statistical testing
- DATA AND CODE AVAILABILITY

SUPPLEMENTAL INFORMATION

Supplemental Information can be found online at https://doi.org/10.1016/j.celrep.2020.03.076.

ACKNOWLEDGMENTS

The Switch Laboratory was supported by grants from the European Research Council under European Union Horizon 2020 Framework Program ERC grant agreement 647458 (MANGO) (to J.S.); the Flanders Institute for Biotechnology (VIB, grant no. C0401); the Industrial Research Fund of KU Leuven ("Industrieel Onderzoeksfonds"); the Funds for Scientific Research Flanders (FWO; Hercules Foundation grant AKUL/15/34 - G0H1716N); the Flanders Agency for Innovation by Science and Technology (IWT; SBO grant 60839); and the Federal Office for Scientific Affairs of Belgium (Belspo; IAP grant P7/16). C.U. was supported by KU Leuven Financiering C14/17/093. N.L. was funded by Fund for Scientific Research Flanders Post-doctoral Fellowship (FWO 12P0919N to N.L.). We acknowledge SOLEIL for providing synchrotron radiation facilities under proposal number 20160142, and we would like to thank the PROXIMA-I team for assistance with using their beamline. Béla Z. Schmidt (KU Leuven) helped with editing the manuscript.

AUTHOR CONTRIBUTIONS

Conceptualization, F.R., J.S., T.L., and R.G.; Methodology and Investigation, T.L., R.G., R.v.d.K., N.L., E.M., R.D.-R., B.H., R.C., H.W., T.G., and J.V.D.; Writing – Original Draft, T.L., J.S., and F.R.; Writing – Review & Editing, T.L., J.S., F.R., R.G., and C.U.; Funding Acquisition, J.S. and F.R.; Resources, F.R., J.S., and C.U.; Supervision, F.R. and J.S.

DECLARATION OF INTERESTS

F.R. and J.S. are scientific founders of Aelin Therapeutics and members of its scientific advisory board.

Received: September 18, 2019
Revised: January 12, 2020
Accepted: March 23, 2020
Published: April 14, 2020

REFERENCES

Adams, P.D., Afonine, P.V., Bunkóczi, G., Chen, V.B., Davis, I.W., Echols, N., Headd, J.J., Hung, L.W., Kapral, G.J., Grosse-Kunstleve, R.W., et al. (2010). PHENIX: a comprehensive Python-based system for macromolecular structure solution. Acta Crystallogr. D Biol. Crystallogr. *66*, 213–221.

Al-Garawi, Z.S., McIntosh, B.A., Neill-Hall, D., Hatimy, A.A., Sweet, S.M., Bagley, M.C., and Serpell, L.C. (2017). The amyloid architecture provides a scaffold for enzyme-like catalysts. Nanoscale *9*, 10773–10783.

Anfinsen, C.B. (1973). Principles that govern the folding of protein chains. Science *181*, 223–230.

Anfinsen, C.B., and Haber, E. (1961). Studies on the reduction and re-formation of protein disulfide bonds. J. Biol. Chem. *236*, 1361–1363.

Bada, J.L. (2013). New insights into prebiotic chemistry from Stanley Miller's spark discharge experiments. Chem. Soc. Rev. *42*, 2186–2196.

Benilova, I., Karran, E., and De Strooper, B. (2012). The toxic Aβ oligomer and Alzheimer's disease: an emperor in need of clothes. Nat. Neurosci. *15*, 349–357.

Boija, A., Klein, I.A., Sabari, B.R., Dall'Agnese, A., Coffey, E.L., Zamudio, A.V., Li, C.H., Shrinivas, K., Manteiga, J.C., Hannett, N.M., et al. (2018). Transcription Factors Activate Genes through the Phase-Separation Capacity of Their Activation Domains. Cell *175*, 1842–1855.e16.

Boke, E., Ruer, M., Wühr, M., Coughlin, M., Lemaitre, R., Gygi, S.P., Alberti, S., Drechsel, D., Hyman, A.A., and Mitchison, T.J. (2016). Amyloid-like Self-Assembly of a Cellular Compartment. Cell *166*, 637–650.

Braun, S., Humphreys, C., Fraser, E., Brancale, A., Bochtler, M., and Dale, T.C. (2011). Amyloid-associated nucleic acid hybridisation. PLoS ONE *6*, e19125.

Breydo, L., and Uversky, V.N. (2015). Structural, morphological, and functional diversity of amyloid oligomers. FEBS Lett. *589* (*19 Pt A*), 2640–2648.

Buck, P.M., Kumar, S., and Singh, S.K. (2013). On the role of aggregation prone regions in protein evolution, stability, and enzymatic catalysis: insights from diverse analyses. PLoS Comput. Biol. *9*, e1003291.

Castillo, V., and Ventura, S. (2009). Amyloidogenic regions and interaction surfaces overlap in globular proteins related to conformational diseases. PLoS Comput. Biol. *5*, e1000476.

Chandonia, J.M., Fox, N.K., and Brenner, S.E. (2017). SCOPe: Manual Curation and Artifact Removal in the Structural Classification of Proteins - extended Database. J. Mol. Biol. *429*, 348–355.

Chen, V.B., Arendall, W.B., 3rd, Headd, J.J., Keedy, D.A., Immormino, R.M., Kapral, G.J., Murray, L.W., Richardson, J.S., and Richardson, D.C. (2010). MolProbity: all-atom structure validation for macromolecular crystallography. Acta Crystallogr. D Biol. Crystallogr. *66*, 12–21.

Chiti, F., and Dobson, C.M. (2017). Protein Misfolding, Amyloid Formation, and Human Disease: A Summary of Progress Over the Last Decade. Annu. Rev. Biochem. *86*, 27–68.

Ciryam, P., Kundra, R., Morimoto, R.I., Dobson, C.M., and Vendruscolo, M. (2015). Supersaturation is a major driving force for protein aggregation in neurodegenerative diseases. Trends Pharmacol. Sci. *36*, 72–77.

Cohen, S.I., Linse, S., Luheshi, L.M., Hellstrand, E., White, D.A., Rajah, L., Otzen, D.E., Vendruscolo, M., Dobson, C.M., and Knowles, T.P. (2013). Proliferation of amyloid-β42 aggregates occurs through a secondary nucleation mechanism. Proc. Natl. Acad. Sci. USA *110*, 9758–9763.

Dale, T. (2006). Protein and nucleic acid together: a mechanism for the emergence of biological selection. J. Theor. Biol. *240*, 337–342.

Das, A., and Makarov, D.E. (2016). Effect of Mutation on an Aggregation-Prone Segment of p53: From Monomer to Dimer to Multimer. J. Phys. Chem. B *120*, 11665–11673.

De Baets, G., Van Durme, J., Rousseau, F., and Schymkowitz, J. (2014). A genome-wide sequence-structure analysis suggests aggregation gatekeepers constitute an evolutionary constrained functional class. J. Mol. Biol. *426*, 2405–2412.

De Smet, F., Saiz Rubio, M., Hompes, D., Naus, E., De Baets, G., Langenberg, T., Hipp, M.S., Houben, B., Claes, F., Charbonneau, S., et al. (2017). Nuclear inclusion bodies of mutant and wild-type p53 in cancer: a hallmark of p53 inactivation and proteostasis remodeling by p53 aggregation. J. Pathol. *242*, 24–38.

Dill, K.A., Ozkan, S.B., Shell, M.S., and Weikl, T.R. (2008). The protein folding problem. Annu. Rev. Biophys. *37*, 289–316.

Dobson, C.M., Knowles, T.P.J., and Vendruscolo, M. (2020). The Amyloid Phenomenon and Its Significance in Biology and Medicine. Cold Spring Harb. Perspect. Biol. *12*, a033878.

Domanov, Y.A., and Kinnunen, P.K. (2008). Islet amyloid polypeptide forms rigid lipid-protein amyloid fibrils on supported phospholipid bilayers. J. Mol. Biol. *376*, 42–54.

Eisenberg, D.S., and Sawaya, M.R. (2017). Structural Studies of Amyloid Proteins at the Molecular Level. Annu. Rev. Biochem. *86*, 69–95.

Eisenberg, D., Weiss, R.M., and Terwilliger, T.C. (1984). The hydrophobic moment detects periodicity in protein hydrophobicity. Proc. Natl. Acad. Sci. USA *81*, 140–144.

Emsley, P., Lohkamp, B., Scott, W.G., and Cowtan, K. (2010). Features and development of Coot. Acta Crystallogr. D Biol. Crystallogr. *66*, 486–501.

Evans, P.R., and Murshudov, G.N. (2013). How good are my data and what is the resolution? Acta Crystallogr. D Biol. Crystallogr. *69*, 1204–1214.

Fernandez-Escamilla, A.M., Rousseau, F., Schymkowitz, J., and Serrano, L. (2004). Prediction of sequence-dependent and mutational effects on the aggregation of peptides and proteins. Nat. Biotechnol. *22*, 1302–1306.

Fitzpatrick, A.W., Knowles, T.P.J., Waudby, C.A., Vendruscolo, M., and Dobson, C.M. (2011). Inversion of the balance between hydrophobic and hydrogen bonding interactions in protein folding and aggregation. PLoS Comput. Biol. *7*, e1002169.

Fowler, D.M., Koulov, A.V., Balch, W.E., and Kelly, J.W. (2007). Functional amyloid–from bacteria to humans. Trends Biochem. Sci. *32*, 217–224.

Fu, L., Niu, B., Zhu, Z., Wu, S., and Li, W. (2012). CD-HIT: accelerated for clustering the next-generation sequencing data. Bioinformatics *28*, 3150–3152.

Ganesan, A., Siekierska, A., Beerten, J., Brams, M., Van Durme, J., De Baets, G., Van der Kant, R., Gallardo, R., Ramakers, M., Langenberg, T., et al. (2016). Structural hot spots for the solubility of globular proteins. Nat. Commun. *7*, 10816.

Geller, R., Pechmann, S., Acevedo, A., Andino, R., and Frydman, J. (2018). Hsp90 shapes protein and RNA evolution to balance trade-offs between protein stability and aggregation. Nat. Commun. *9*, 1781.

Goldberg, T., Hecht, M., Hamp, T., Karl, T., Yachdav, G., Ahmed, N., Altermann, U., Angerer, P., Ansorge, S., Balasz, K., et al. (2014). LocTree3 prediction of localization. Nucleic Acids Res. *42*, W350-5.

Gray, V.E., Hause, R.J., and Fowler, D.M. (2017). Analysis of Large-Scale Mutagenesis Data To Assess the Impact of Single Amino Acid Substitutions. Genetics *207*, 53–61.

Greenwald, J., and Riek, R. (2012). On the possible amyloid origin of protein folds. J. Mol. Biol. *421*, 417–426.

Greenwald, J., Friedmann, M.P., and Riek, R. (2016). Amyloid Aggregates Arise from Amino Acid Condensations under Prebiotic Conditions. Angew. Chem. Int. Ed. Engl. *55*, 11609–11613.

Hatos, A., Hajdu-Soltesz, B., Monzon, A.M., Palopoli, N., Álvarez, L., Aykac-Fas, B., Bassot, C., Benítez, G.I., Bevilacqua, M., Chasapi, A., et al. (2020). DisProt: intrinsic protein disorder annotation in 2020. Nucleic Acids Res. *48*, D269–D276.

Henne, A., Brüggemann, H., Raasch, C., Wiezer, A., Hartsch, T., Liesegang, H., Johann, A., Lienard, T., Gohl, O., Martinez-Arias, R., et al. (2004). The genome sequence of the extreme thermophile Thermus thermophilus. Nat. Biotechnol. *22*, 547–553.

Hipp, M.S., Kasturi, P., and Hartl, F.U. (2019). The proteostasis network and its decline in ageing. Nat. Rev. Mol. Cell Biol. *20*, 421–435.

Horwich, A.L., Neupert, W., and Hartl, F.U. (1990). Protein-catalysed protein folding. Trends Biotechnol. *8*, 126–131.

Iadanza, M.G., Jackson, M.P., Hewitt, E.W., Ranson, N.A., and Radford, S.E. (2018). A new era for understanding amyloid structures and disease. Nat. Rev. Mol. Cell Biol. *19*, 755–773.

Ivnitski, D., Amit, M., Rubinov, B., Cohen-Luria, R., Ashkenasy, N., and Ashkenasy, G. (2014). Introducing charge transfer functionality into prebiotically relevant β-sheet peptide fibrils. Chem. Commun. (Camb.) *50*, 6733–6736.

Jahn, T.R., and Radford, S.E. (2008). Folding versus aggregation: polypeptide conformations on competing pathways. Arch. Biochem. Biophys. *469*, 100–117.

Jayaraj, G.G., Hipp, M.S., and Hartl, F.U. (2020). Functional Modules of the Proteostasis Network. Cold Spring Harb. Perspect. Biol. *12*, a033951.

Kabsch, W. (2010). Xds. Acta Crystallogr. D Biol. Crystallogr. *66*, 125–132.

Kerner, M.J., Naylor, D.J., Ishihama, Y., Maier, T., Chang, H.C., Stines, A.P., Georgopoulos, C., Frishman, D., Hayer-Hartl, M., Mann, M., and Hartl, F.U. (2005). Proteome-wide analysis of chaperonin-dependent protein folding in Escherichia coli. Cell *122*, 209–220.

Kitayner, M., Rozenberg, H., Kessler, N., Rabinovich, D., Shaulov, L., Haran, T.E., and Shakked, Z. (2006). Structural basis of DNA recognition by p53 tetramers. Mol. Cell *22*, 741–753.

Konagurthu, A.S., Whisstock, J.C., Stuckey, P.J., and Lesk, A.M. (2006). MUSTANG: a multiple structural alignment algorithm. Proteins *64*, 559–574.

Kumar, S., Stecher, G., Suleski, M., and Hedges, S.B. (2017). TimeTree: A Resource for Timelines, Timetrees, and Divergence Times. Mol. Biol. Evol. *34*, 1812–1819.

Labbadia, J., and Morimoto, R.I. (2015). The biology of proteostasis in aging and disease. Annu. Rev. Biochem. *84*, 435–464.

Laganowsky, A., Liu, C., Sawaya, M.R., Whitelegge, J.P., Park, J., Zhao, M., Pensalfini, A., Soriaga, A.B., Landau, M., Teng, P.K., et al. (2012). Atomic view of a toxic amyloid small oligomer. Science *335*, 1228–1231.

Landreh, M., Sawaya, M.R., Hipp, M.S., Eisenberg, D.S., Wüthrich, K., and Hartl, F.U. (2016). The formation, function and regulation of amyloids: insights from structural biology. J. Intern. Med. *280*, 164–176.

Lee, Y., Zhou, T., Tartaglia, G.G., Vendruscolo, M., and Wilke, C.O. (2010). Translationally optimal codons associate with aggregation-prone sites in proteins. Proteomics *10*, 4163–4171.

Leuenberger, P., Ganscha, S., Kahraman, A., Cappelletti, V., Boersema, P.J., von Mering, C., Claassen, M., and Picotti, P. (2017). Cell-wide analysis of protein thermal unfolding reveals determinants of thermostability. Science *355*, 6327.

Linding, R., Schymkowitz, J., Rousseau, F., Diella, F., and Serrano, L. (2004). A comparative study of the relationship between protein structure and beta-aggregation in globular and intrinsically disordered proteins. J. Mol. Biol. *342*, 345–353.

Macedo, B., and Cordeiro, Y. (2017). Unraveling Prion Protein Interactions with Aptamers and Other PrP-Binding Nucleic Acids. Int. J. Mol. Sci. *18*, 5.

Mahalka, A.K., Maury, C.P.J., and Kinnunen, P.K.J. (2011). 1-Palmitoyl-2-(9′-oxononanoyl)-sn-glycero-3-phosphocholine, an oxidized phospholipid, accelerates Finnish type familial gelsolin amyloidosis in vitro. Biochemistry *50*, 4877–4889.

Maury, C.P. (2009). Self-propagating beta-sheet polypeptide structures as prebiotic informational molecular entities: the amyloid world. Orig. Life Evol. Biosph. *39*, 141–150.

Maury, C.P. (2015). Origin of life. Primordial genetics: Information transfer in a pre-RNA world based on self-replicating beta-sheet amyloid conformers. J. Theor. Biol. *382*, 292–297.

McCoy, A.J. (2007). Solving structures of protein complexes by molecular replacement with Phaser. Acta Crystallogr. D Biol. Crystallogr. *63*, 32–41.

Miller, S.L. (1953). A production of amino acids under possible primitive earth conditions. Science *117*, 528–529.

Monsellier, E., and Chiti, F. (2007). Prevention of amyloid-like aggregation as a driving force of protein evolution. EMBO Rep. *8*, 737–742.

Murshudov, G.N., Skubák, P., Lebedev, A.A., Pannu, N.S., Steiner, R.A., Nicholls, R.A., Winn, M.D., Long, F., and Vagin, A.A. (2011). REFMAC5 for the refinement of macromolecular crystal structures. Acta Crystallogr. D Biol. Crystallogr. *67*, 355–367.

Natan, E., Baloglu, C., Pagel, K., Freund, S.M.V., Morgner, N., Robinson, C.V., Fersht, A.R., and Joerger, A.C. (2011). Interaction of the p53 DNA-binding domain with its n-terminal extension modulates the stability of the p53 tetramer. J. Mol. Biol. *409*, 358–368.

Omosun, T.O., Hsieh, M.C., Childers, W.S., Das, D., Mehta, A.K., Anthony, N.R., Pan, T., Grover, M.A., Berland, K.M., and Lynn, D.G. (2017). Catalytic diversity in self-propagating peptide assemblies. Nat. Chem. *9*, 805–809.

Otzen, D., and Riek, R. (2019). Functional Amyloids. Cold Spring Harb. Perspect. Biol. *11*, a033860.

Parker, E.T., Zhou, M., Burton, A.S., Glavin, D.P., Dworkin, J.P., Krishnamurthy, R., Fernández, F.M., and Bada, J.L. (2014). A plausible simultaneous synthesis of amino acids and simple peptides on the primordial Earth. Angew. Chem. Int. Ed. Engl. *53*, 8132–8136.

Potterton, L., Agirre, J., Ballard, C., Cowtan, K., Dodson, E., Evans, P.R., Jenkins, H.T., Keegan, R., Krissinel, E., Stevenson, K., et al. (2018). CCP4i2: the new graphical user interface to the CCP4 program suite. Acta Crystallogr. D Struct. Biol. *74*, 68–84.

Prakash, A., Jeffryes, M., Bateman, A., and Finn, R.D. (2017). The HMMER Web Server for Protein Sequence Similarity Search. Curr. Protoc. Bioinformatics *60*, 3.15.1–3.15.23.

Ramakrishnan, R., Houben, B., Kreft, L., Botzki, A., Schymkowitz, J., and Rousseau, F. (2020). Protein Homeostasis Database: protein quality control in E. coli. Bioinformatics *36*, 948–949.

Reumers, J., Maurer-Stroh, S., Schymkowitz, J., and Rousseau, F. (2009). Protein sequences encode safeguards against aggregation. Hum. Mutat. *30*, 431–437.

Rousseau, F., Serrano, L., and Schymkowitz, J.W. (2006). How evolutionary pressure against protein aggregation shaped chaperone specificity. J. Mol. Biol. *355*, 1037–1047.

Rout, S.K., Friedmann, M.P., Riek, R., and Greenwald, J. (2018). A prebiotic template-directed peptide synthesis based on amyloids. Nat. Commun. *9*, 234.

Schymkowitz, J., Borg, J., Stricher, F., Nys, R., Rousseau, F., and Serrano, L. (2005). The FoldX web server: an online force field. Nucleic Acids Res. *33*, W382-8.

Scior, A., Juenemann, K., and Kirstein, J. (2016). Cellular strategies to cope with protein aggregation. Essays Biochem. *60*, 153–161.

Smoot, M.E., Ono, K., Ruscheinski, J., Wang, P.L., and Ideker, T. (2011). Cytoscape 2.8: new features for data integration and network visualization. Bioinformatics *27*, 431–432.

Soragni, A., Janzen, D.M., Johnson, L.M., Lindgren, A.G., Thai-Quynh Nguyen, A., Tiourin, E., Soriaga, A.B., Lu, J., Jiang, L., Faull, K.F., et al. (2016). A Designed Inhibitor of p53 Aggregation Rescues p53 Tumor Suppression in Ovarian Carcinomas. Cancer Cell *29*, 90–103.

Tartaglia, G.G., Pechmann, S., Dobson, C.M., and Vendruscolo, M. (2007). Life on the edge: a link between gene expression levels and aggregation rates of human proteins. Trends Biochem. Sci. *32*, 204–206.

Tena-Solsona, M., Nanda, J., Díaz-Oltra, S., Chotera, A., Ashkenasy, G., and Escuder, B. (2016). Emergent Catalytic Behavior of Self-Assembled Low Molecular Weight Peptide-Based Aggregates and Hydrogels. Chemistry *22*, 6687–6694.

Uniprot, C.; UniProt Consortium (2008). The universal protein resource (UniProt). Nucleic Acids Res. *36*, D190–D195.

van der Kant, R., Karow-Zwick, A.R., Van Durme, J., Blech, M., Gallardo, R., Seeliger, D., Aßfalg, K., Baatsen, P., Compernolle, G., Gils, A., et al. (2017). Prediction and Reduction of the Aggregation of Monoclonal Antibodies. J. Mol. Biol. *429*, 1244–1261.

Van Durme, J., De Baets, G., Van Der Kant, R., Ramakers, M., Ganesan, A., Wilkinson, H., Gallardo, R., Rousseau, F., and Schymkowitz, J. (2016). Solubis: a webserver to reduce protein aggregation through mutation. Protein Eng. Des. Sel. *29*, 285–289.

Wang, G., and Fersht, A.R. (2017). Multisite aggregation of p53 and implications for drug rescue. Proc. Natl. Acad. Sci. USA *114*, E2634–E2643.

Wickner, R.B., Edskes, H.K., Shewmaker, F., Kryndushkin, D., and Nemecek, J. (2009). Prion variants, species barriers, generation and propagation. J. Biol. *8*, 47.

Xu, J., Reumers, J., Couceiro, J.R., De Smet, F., Gallardo, R., Rudyak, S., Cornelis, A., Rozenski, J., Zwolinska, A., Marine, J.C., et al. (2011). Gain of function of mutant p53 by coaggregation with multiple tumor suppressors. Nat. Chem. Biol. *7*, 285–295.

STAR★METHODS

KEY RESOURCES TABLE

REAGENT or RESOURCE	SOURCE	IDENTIFIER
Chemicals, Peptides, and Recombinant Proteins		
PWO DNA polymerase	Sigma	11644947001
restriction enzymes Nde1 and BamH1	NEB	R0111 and R3136
HEPES	Merck / Sigma-Aldrich	RDD002
n-octyl-β-D-glucoside	Merck / Sigma-Aldrich	O8001
imidazole	Merck / Sigma-Aldrich	792527
NaCl	Merck / Sigma-Aldrich	S7653
IPTG	Duchefa	DUC.I1401.0025
zinc chloride	Merck / Sigma-Aldrich	229997
beta-mercaptoethanol	Merck / Sigma-Aldrich	6250
DTT	Duchefa	DUC.D1309.0025
Triton X-100	Merck / Sigma-Aldrich	1.08603
sodium deoxycholate	Merck / Sigma-Aldrich	D6750
glycerol	VWR	444485B
ammonium bisulfate	Merck / Sigma-Aldrich	09849
Critical Commercial Assays		
Q5 Site-Directed Mutagenesis Kit	NEB	E0554S
GenElute mammalian total RNA extraction kit	Merck / Sigma-Aldrich	RTN70
RevertAid H Minus First Strand cDNA Synthesis Kit	Thermo Fisher Scientific	K1631
GoTaq Probe qPCR Master Mix	Promega	A6101
Deposited Data		
Structure of p53cc	this paper	PDB: 6SL6
Experimental Models: Cell Lines		
Saos-2	ATCC	ATB-85
Oligonucleotides		
p53 consensus binding site: TGGTGTTTTGCAGGCA TGTCTAGGCATGTCT	this paper	Integrated DNA Technologies
p53 binding site control: TGGTGTTTTGCAGGACGT TCTAGGACGTTCT	this paper	Integrated DNA Technologies
T256R mutagenesis primer forward cccatcctcacca tcatcagactggaagactcc	this paper	Integrated DNA Technologies
T256R mutagenesis primer reverse ggagtcttccagt ctgatgatggtgaggatggg	this paper	Integrated DNA Technologies
L252K (+T256R) mutagenesis primer forward catgaaccggaggcccatcaagaccatcatcagactggaag	this paper	Integrated DNA Technologies
L252K (+T256R) mutagenesis primer reverse cttccagtctgatgatggtcttgatgggcctccggttcatg	this paper	Integrated DNA Technologies
A138G mutagenesis primer forward gttttgccaactg ggcaagacctgccctg	this paper	Integrated DNA Technologies
A138G mutagenesis primer reverse cagggcaggt cttgcccagttggcaaaac	this paper	Integrated DNA Technologies
R267L mutagenesis primer forward tggtaatctact gggactgaacagctttgaggtgc	this paper	Integrated DNA Technologies
R267L mutagenesis primer reverse gcacctcaaag ctgttcagtcccagtagattacca	this paper	Integrated DNA Technologies

(*Continued on next page*)

Continued

REAGENT or RESOURCE	SOURCE	IDENTIFIER
N268D (+R267L) mutagenesis primer forward acgcacctcaaagctgtccagtcccagtagattac	this paper	Integrated DNA Technologies
N268D (+R267L) mutagenesis primer reverse gtaatctactgggactggacagctttgaggtgcgt	this paper	Integrated DNA Technologies
RRM2B qPCR assay forward primer: ggtcttatgc caggactcac	this paper	Integrated DNA Technologies
RRM2B qPCR assay reverse primer: caatgatctc cctgacccttc, probe:ctgtgactttgcttgcctgatgttcc	this paper	Integrated DNA Technologies
RRM2B qPCR assay hydrolysis probe: ctgtgactt tgcttgcctgatgttcc	this paper	Integrated DNA Technologies
TNFRSF10B qPCR assay forward primer: accacgac cagaaacacag	this paper	Integrated DNA Technologies
TNFRSF10B qPCR assay reverse primer: cattcgatgt cactccaggg	this paper	Integrated DNA Technologies
TNFRSF10B qPCR assay hydrolysis probe: acaatca ccgaccttgaccatccc	this paper	Integrated DNA Technologies
TP53INP1 qPCR assay forward primer: ctcattgaac atcccagcatg	this paper	Integrated DNA Technologies
TP53INP1 qPCR assay reverse primer: atttcattttgagc ttccactctg	this paper	Integrated DNA Technologies
TP53INP1 qPCR assay hydrolysis probe: ctgtgcataa ctcctgccctggt	this paper	Integrated DNA Technologies
BAX qPCR assay forward primer: gacatgttttctgac ggc aac	this paper	Integrated DNA Technologies
BAX qPCR assay reverse primer: aagtccaatgtccagccc	this paper	Integrated DNA Technologies
BAX qPCR assay hydrolysis probe: ctggcaaagtagaaa agggcgacaac	this paper	Integrated DNA Technologies
MDM2 qPCR assay forward primer: tgccaagcttctc tgtgaaag	this paper	Integrated DNA Technologies
MDM2 qPCR assay reverse primer: tccttttgatcactc ccacc	this paper	Integrated DNA Technologies
MDM2 qPCR assay hydrolysis probe: acctgagtccga tgattcctgctg	this paper	Integrated DNA Technologies
P21 qPCR assay forward primer: tgtcactgtcttgtacccttg	this paper	Integrated DNA Technologies
P21 qPCR assay reverse primer: ggcgtttggagtggtagaa	this paper	Integrated DNA Technologies
P21 qPCR assay hydrolysis probe: tctgtcatgctggt ctgccgc	this paper	Integrated DNA Technologies
PUMA qPCR assay forward primer: cctaattgggctc catctcg	this paper	Integrated DNA Technologies
PUMA qPCR assay reverse primer: cgacctcaacgca cagtac	this paper	Integrated DNA Technologies
PUMA qPCR assay hydrolysis probe: atcatgggactcc tgcccttac	this paper	Integrated DNA Technologies
Recombinant DNA		
pET15b-TEV with p53 DBD WT	MerckMillipore, this paper	69661-3
pET15b-TEV with p53 DBD CC	MerckMillipore, this paper	69661-3
pCDNA3.1 with full-length p53 WT	Thermo Fisher Scientific / Invitrogen, this paper	V79020
pCDNA3.1 with full-length p53 CC	Thermo Fisher Scientific / Invitrogen, this paper	V79020

(*Continued on next page*)

Continued

REAGENT or RESOURCE	SOURCE	IDENTIFIER
Software and Algorithms		
cd-hit	16731699	http://weizhongli-lab.org/cd-hit/
AliView	25095880	https://github.com/AliView/AliView
AGADIR	7664054	http://agadir.crg.es/
FoldX	15980494	http://foldxsuite.crg.eu/
TANGO	15313629	http://tango.crg.es/
YASARA	YASARA Biosciences GmbH	http://www.yasara.org/
XDS	Kabsch, 2010	http://xds.mpimf-heidelberg.mpg.de/
Phaser	19461840	https://www.phaser.cimr.cam.ac.uk/index.php/Phaser_Crystallographic_Software
Phenix	31588918	https://www.phenix-online.org/
Coot	20383002	https://www2.mrc-lmb.cam.ac.uk/personal/pemsley/coot/
MolProbity	17452350	http://molprobity.biochem.duke.edu/
PyMOL	The PyMOL Molecular Graphics System, Version 2.0 Schrödinger, LLC.	https://pymol.org/2/
REFMAC	25075342	http://www.ccp4.ac.uk/html/refmac5/keywords/xray-principal.html
CCP4i2	29533233	http://www.ccp4.ac.uk/ccp4i2/
Origin	OriginLab	https://www.originlab.com/
Cytoscape	14597658	https://cytoscape.org/
qbase+	17291332	https://www.qbaseplus.com/
R	The R Project for Statistical Computing	https://www.r-project.org/
R Studio	R Studio	https://rstudio.com/
HMMER	29220076	https://www.ebi.ac.uk/Tools/hmmer/search/phmmer
Other		
Transfection reagent	Transit X2	Mirus Bio
Complete protease inhibitor	Merck / Sigma-Aldrich	04693116001

LEAD CONTACT AND MATERIALS AVAILABILITY

Further information and requests for resources and reagents should be directed to and will be fulfilled by the Lead Contact: Frederic Rousseau (frederic.rousseau@kuleuven.be) or by Joost Schymkowitz (joost.schymkowitz@kuleuven.be). All unique/stable reagents generated in this study are available from the Lead Contact with a completed Materials Transfer Agreement.

EXPERIMENTAL MODEL AND SUBJECT DETAILS

Cell culture

Saos-2 cells (ATCC ATB-85, osteosarcoma from a 11-year old female Caucasian) were cultured in DMEM with 10% fetal bovine serum (GIBCO) with minimum non-essential amino acid and sodium pyruvate supplements (GIBCO) in a cell culture incubator at 5% CO_2 and 37°C. The cells were obtained directly from ATCC, expanded and vials were kept in cryostorage. A fresh vial of cryo-preserved cells was thawed out after every 20 passages. The identity of the line was monitored by the absence of p53.

METHOD DETAILS

Transfection

1.5 μg DNA and 4.5 μL transfection reagent (TransIT X2, Mirus Bio) per reaction were mixed in 200 μL OptiMEM medium (GIBCO), incubated for at least 10 min and then added to 2 mL of a cell suspension at 150000 cells/ml in 6well plates. Cells were harvested 20-24 hours later.

Cloning and mutation of p53 DBD

Mutations A138G, L252K, T256R, R267L and N268D were generated by QuickChange PCR in the CDS of full-length p53 in the pCDNA3 backbone. For protein purification the mutated and wt DBD were amplified (residues 89-311) by PCR and cloned (Nde1/BamH1) into a modified version of the vector pET15b containing an N-terminal HIS-tag followed by a TEV-protease cleavage site (pET15b-TEV). For transfection, the full-length p53 versions in the pCDNA3.1 backbone were used.

Protein expression and purification

Production of p53 DBD wt or cc was induced from an overnight starter culture of freshly transformed *E. coli* strain NiCo21 (DE3) (NEB) at an OD of 0.8 to 1.0 with 1 mM IPTG at 28°C o/n in the presence of 20 μM $ZnCl_2$. The next day, cells were lysed (in 50 mM HEPES, 300 mM NaCl, 3% glycerol, 5 mM beta-mercaptoethanol and protease inhibitors) using a French Press, followed by sonification and centrifugation at 40,000 g for 30 min. The p53 DBD was purified from the supernatant by IMAC (HisTrapFF 5 ml, GE Healthcare), followed by size exclusion on a HiLoad 26/60 Superdex 75 column (Amersham Biosciences) on an Äkta Pure system (GE Healthcare) in 50 mM HEPES, 300 mM NaCl, 5 mM DTT and 10 mM ammonium bisulfate. The insoluble fraction was purified from the pellet after centrifugation by several washes in increasing detergent concentration (Triton X-100 and sodium deoxycholate), and finally by dissolving in buffered 8 M urea, followed by IMAC. Protein identity was verified by mass spectrometry.

Crystallization and structure determination

Purified p53cc was dialyzed against buffer C (50 mM HEPES, 50 mM NaCl, 10 mM DTT, pH 7.5) containing 0.4% w/v n-octyl-β-D-glucoside for 24 hours at 4°C. After dialysis, the protein was concentrated to 5.1 mg/ml using centrifugal concentrators of MWCO 3000 Da (Millipore) operated at 3500 g at 4°C. The concentrated protein stock was filtered through 0.2 um PVDF filters (Millipore) and kept on ice until use. Crystallization screenings were carried out using the sitting-drop vapor diffusion method and several commercially available crystallization screens from Hampton Research (California, U.S.A.) and Molecular Dimensions (Suffolk, UK). To this end 100 nL drops of protein stock were dispensed and mixed 1:1 with crystallization buffer using a Mosquito nanoliter crystallization robot (TTP Labtech, Melbourn, UK) and incubated at either 4°C or 20°C. Rod-shape crystals appeared after one week and grew to > 50 μm in the longest axis direction over four weeks at 4°C in the following condition: 200 mM ammonium citrate tribasic pH 7.0, 20% w/v polyethylene glycol 3350 (H4 condition of Index screen, Hampton Research). Crystals were flash-cooled in liquid nitrogen after a quick passage through cryo-protection solution (75% crystallization solution plus 25% glycerol). X-ray diffraction data were collected to a resolution of 1.67 Å at the PROXIMA-I beam line of the SOLEIL synchrotron (Saint-Aubin, France). Data were indexed, integrated and scaled with XDS (Kabsch, 2010), and merged with Aimless (Evans and Murshudov, 2013). The phase problem was solved by molecular replacement using Phaser (McCoy, 2007) and the p53 wt structure 2XWR (Natan et al., 2011) as a search model. Only the A chain of 2XWR, of which metal ions and water molecules were removed, was used in molecular replacement. The molecular replacement solution was refined by iterative cycles of manual structure building using Coot (Emsley et al., 2010) and REFMAC5 (Murshudov et al., 2011) until R-factors converged to 16.4% and 18.0% (R_{work} and R_{free}, respectively). Structure validation was done using MOLPROBITY (Chen et al., 2010) and a final round of structure refinement was carried out in PHENIX (Adams et al., 2010). All figures were prepared using PyMOL (Schrödinger). Aimless, Phaser, REFMAC5 and Coot were used as implemented in CCP4i2 (Potterton et al., 2018). The full statistics of structure building and refinement can be seen in Table S1. The PDB accession code for the p53cc structure is 6SL6.

Dynamic light scattering

Purified protein was diluted to 0.25 mg/ml (in 50 mM HEPES, 300 mM NaCl, 5 mM DTT, 10 mM ammonium bisulfate), filtered using 0.1 mM syringe-tip PVDF filters and measured in a flat-bottom 96-well microclear plate (Greiner, Frickenhausen, Germany) on a Wyatt DynaPro plate reader equipped with a 830 nm laser source (Wyatt, Santa Barbara, CA, USA) every 5 min with auto-attenuation of laser power.

ThT and pFTAA binding

Purified protein was filtered through 0.1 mM PVDF filters, concentrated to 1 mg/ml and dye binding was measured on a FluoStar plate reader in a flat-bottom 96-well microclear plate (Greiner, Frickenhausen, Germany) every 5 min with 30 s shaking prior to each measurement. Filter settings: 440-10 nm excitation / 480-10 nm emission for ThT and 480-10 nm excitation / 520-10 nm emission for pFTAA.

Fluorescence anisotropy

Fluorescence anisotropy (FA) was recorded at room temperature in a FlexStation 3 (Molecular Devices, USA) and a PolarStar Optima plate reader (BMG labtech, Germany), with 490 nm excitation and 525 nm emission filters, using 10 nm band-pass. DNA binding affinities were determined as monitored changes in the anisotropy of 5′-Alexa488-labeled oligomers containing the consensus binding sequence (5′-TGGTGTTTTGCAGGCATGTCTAGGCATGTCT-3′), as well as the control sequence (5′-TGGTGTTTTGCAGGACGTTCTAG GACGTTCT-3′). Measurements were obtained in 50 mM HEPES (pH 7.5), 0.2 M NaCl and 5 mM dithiothreitol (DTT), containing 0.2% Tween20 and 0.4% PEG_{400}. Protein concentration was varied up to 70 μM and labeled-DNA concentration was fixed at 25 nM.

Dissociation constants were calculated by fitting the anisotropy (A) experimental data to a one-site binding model to the following quadratic equation:

$$A = A_0 + A_T \frac{([L] + K_D + [R]) - \sqrt{([L] + K_D + [R])^2 - 4[L][R]}}{2}$$

where A_0 and A_T are the initial and total fluorescence, K_D is the equilibrium constant, [R] is the protein concentration and [L] is the DNA oligomer concentration.

Microscale thermophoresis

DNA binding affinities of the WT DBD domain, as well as the mutant were also determined with microscale thermophoresis (MST). DNA oligomer concentration was kept constant at 25 nM, whereas both proteins were titrated down from 70 μM. Buffer composition was similar to FA measurements. Measurements were recorded on a Monolith NT automated instrument (NanoTemper Technologies GmbH, Germany) with a blue-laser channel at 40% LED excitation power and 60% MST power at ambient conditions. Affinity constants and experimental data fitting was performed using the NanoTemper analysis software (v2.2.4). The thermophoretic movement of bound and unbound state superpose linearly, therefore the fraction bound (f) is described as:

$$F_{norm} = (1 - f)F_{norm,unbound} + (f)F_{norm,bound}$$

where F_{norm} is the normalized fluorescence, $F_{norm,\ unbound}$ corresponds to normalized fluorescence of the unbound state and $F_{norm,\ bound}$ is the normalized fluorescence of the bound state.

Quantitative PCR

Cells were lysed for at least 15 min on ice in 300 μL lysis buffer (1% NP40 in PBS with nuclease (Pierce Universal Nuclease for Cell Lysis)). After centrifugation at 4°C for 15 min in a table-top centrifuge, RNA was extracted from the supernatant using the GenElute mammalian total RNA extraction kit with on-column DNase treatment (Sigma). RNA was reverse transcribed using RevertAid H Minus First Strand cDNA Synthesis Kit (Thermo Fisher Scientific). Quantitative PCR was carried out with 6FAM or HEX-labeled probe/primer mixes (ZEN/IBFQ quenched, Integrated DNA Technologies) and GoTaq Probe qPCR Master Mix (Promega) in a C1000Touch/CFX96 cycler (BioRad) using the following settings: 20 s 95°C (1 cycle), 5 s 95°C, 25 s 60°C (40 cycles). Primers and probes were designed using the RealTime qPCR Assay tool (Integrated DNA Technologies). Data were analyzed in qbase+ (Biogazelle) with normalization to two reference genes out of eight tested that performed best in the geNorm analysis in qbase+.

QUANTIFICATION AND STATISTICAL ANALYSIS

SCOPe analysis and artificial protein datasets

The entire SCOPe database (release 2.06; Chandonia et al., 2017) was filtered at 40% identity using cd-hit (Fu et al., 2012), sequences with gaps were removed and finally, because the subject of this study are single chain globular proteins, all folds not belonging to SCOPe classes a (all alpha), b (all beta), c (alpha and beta interspersed - α/β) or d (alpha and beta largely separated - α+β) were removed. Average hydrophobicity per fold was determined according to the Eisenberg scale using a custom plugin to the AGADIR algorithm (Eisenberg et al., 1984).

Evolutionary analysis of p53

Residues 89-311 of the human p53 protein were used to run HMMER (Prakash et al., 2017) (EMBL-EBI) against the UniProtKB (Uniprot, 2008) at significance E-values for sequence and hit of 0.01 and 0.03, respectively. The initial 1294 hits were reduced to 337 by running cd-hit at 95% sequence identity and further manual curation using AliView, removing all sequences with large gaps at or near the ILTIITL APR or lacking more than one of the conserved Zn-coordinating residues of p53 family proteins. Phylogenetic information was extracted from the UniProtKB.

PDB entries of APRs and corresponding full-length protein structures

Protein	APR	Full-length	PMIDs
Bloom syndrome protein	L. Serpell, personal communication	4O3M	23252554, 24816114
Transthyretin	4XFN	4QXV	26459562, 26020516
Insulin	3HYD	5E7W	19864624, 29086855
SOD1	5DLI, 4NIN, 4NIP	2C9V	29453800, 24344300, 16406071
Tp53	4RP6	2XWR	26748848, 21457718
β2-microglobulin	3LOZ, 4E0K, 4E0L	2YXF	21131979, 23213214, 17646174
Lysozyme	4R0P	2NWD	25474758, 17360367

Deep mutational scanning analysis for suppressing mutations

Deep mutational scanning information was retrieved from earlier work by Gray et al. (2017). This dataset combines several studies in which protein fitness was assessed upon exhaustive mutations in virtually every position in the primary protein sequence. Gray et al. (2017) gathered these data and performed normalizations on the fitness scores therein, yielding a large database of the effects of amino acid substitutions spanning 10 different proteins. In this dataset, we identified APRs using the TANGO algorithm, after which each APR position was mutated to all other amino acids, and reanalysed through TANGO. Mutations were then classified as ''suppressing'' when they fully disrupted their parent APR. Next, suppressing mutations were cross-referenced with the deep mutational scanning data to find suppressing mutations for which a fitness score was actually reported. Finally, structure files for each protein were obtained from the PDB, and the list of suppressing mutations was further filtered on their occurrence in a pdb-structure. These filtering steps resulted in a list of 14 APRs from 3 different proteins (uniport IDs P02829, P28482 and P62593), for which a total of 664 suppressing mutations were identified. To analyze the structural effects of these mutations, the corresponding pdb-structures (2cg9, 2y9q and 1erm, respectively) were first repaired in FoldX using the RepairPDB command, after which stability effects of mutations were predicted using the Buildmodel command, with default settings. Statistical analyses on and visualization of these data were performed using the R statistical computing software. The source files and R-scripts used are available in the files Data S1 (Source files) and Data S2 (R-scripts).

Codon usage correlation analysis

Individual weights were attributed to codon transitions induced by single-nucleotide mutation events ($AA_{transition}$), using:

$$AA_{transition} = \sum_{i=0}^{n} freq(i)_{perAA} * C\ (i)_{prop}$$

where $freq_{perAA}$ is the codon frequency usage per residue, C_{prop} corresponds to the number of possible single-mutation codon transitions per property (referring to residue side chain physicochemical properties or aggregation propensity) and n is the number of codons encoding for a single amino acid. Network construction and analysis was performed utilizing Cytoscape 3 (Smoot et al., 2011).

Statistical testing

Normality was assessed both visually (using R's hist and qqnorm functions) and by using the Shapiro test for normality (R function shapiro.test). Significance of the difference between the mean of two groups was then either calculated using Student's unpaired t test for normal or near-normal distributions, or the unpaired Wilcoxon-Mann-Whitney U test for non-normal distributions (R functions t.test and wilcox.test, respectively). Significance is denoted as '***', p value between 0 and 0.001; '**' p value between 0.001 and 0.01; '*', p value between 0.01 and 0.05; 'n.s.', p value > 0.05.

DATA AND CODE AVAILABILITY

The crystallographic dataset generated during this study is available at the Protein Data Bank (https://www.rcsb.org/) under ID 6SL6.

Cell Reports, Volume *31*

Supplemental Information

Thermodynamic and Evolutionary Coupling between the Native and Amyloid State of Globular Proteins

Tobias Langenberg, Rodrigo Gallardo, Rob van der Kant, Nikolaos Louros, Emiel Michiels, Ramon Duran-Romaña, Bert Houben, Rafaela Cassio, Hannah Wilkinson, Teresa Garcia, Chris Ulens, Joost Van Durme, Frederic Rousseau, and Joost Schymkowitz

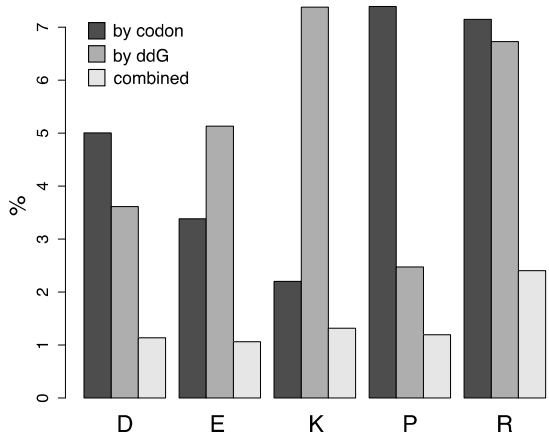

Supplementary Figure 1. Percent chance of placing a gatekeeper residue in an APR based on codon usage or stability (by ddG), or both combined. Related to Figure 3.

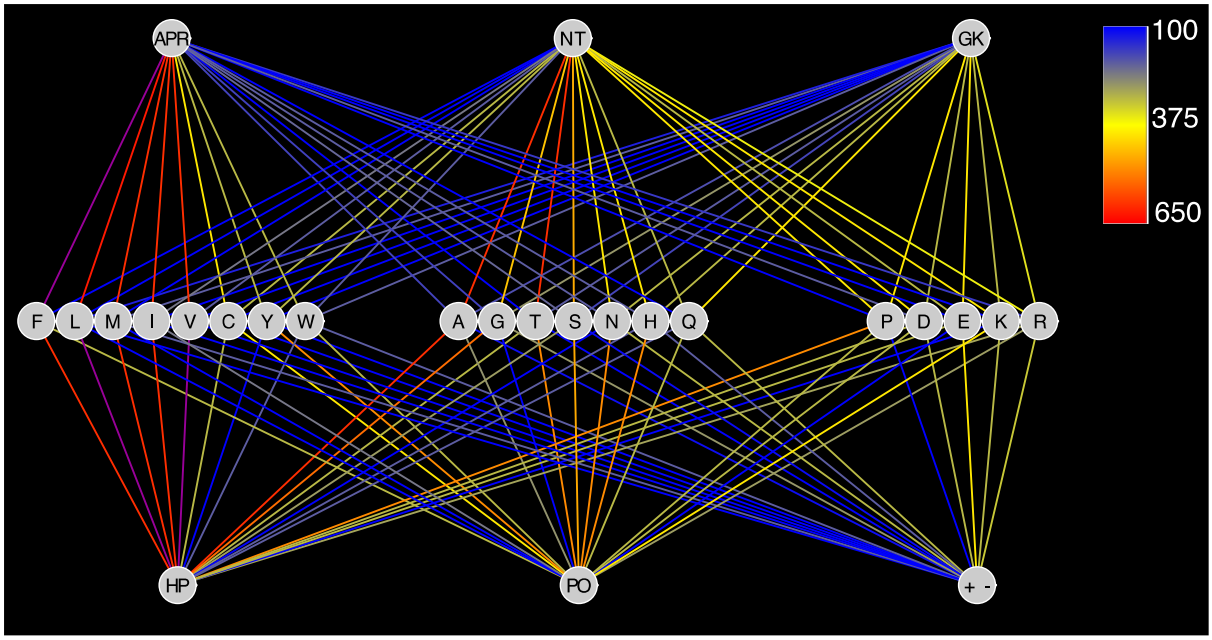

Supplementary Figure 2. Network mapping of single nucleotide based transitional propensities related to physicochemical stability (bottom half) and aggregation proclivity (top half) of the 20 amino acid residue side chains. Related to Figure 3. Top row nodes categorise mutational transitions as aggregation-prone, neutral or gatekeepers, whereas the bottom row is represented by nodes for transitions to hydrophobic, polar or charged states. Initial residue states are shown in single letter coding as the central node row of the graph. Network edges are colour-coded based on strength of transitional propensity (red to blue gradient). Single nucleotide mutations rarely switch to codons encoding for residues with altered physicochemical properties and this conservation is even stronger regarding the amyloid propensity of the transitional residues. This codon bias conservation highlights the coupling between aggregation propensity and globular stability of amino acid side chains.

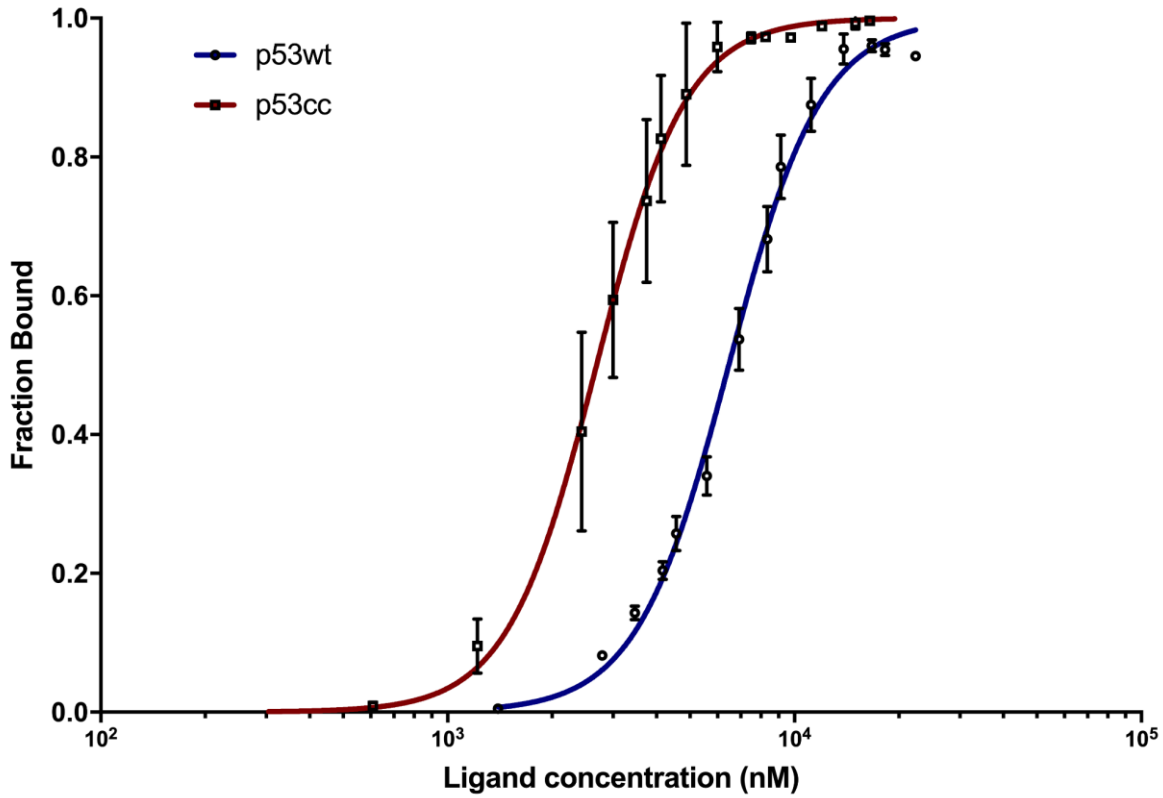

Supplementary Figure 3. DNA-binding curves of p53cc and wt measured with microscale thermophoresis (MST). Related to Figure 5. Raw fluorescence is normalized to the fraction of bound target shown in the vertical axis. Similar affinities were calculated for both p53cc and wt constructs (2.69 μM ± 0.67 μM and 6.47 μM ± 0.70 μM, respectively). Measurements were carried out in triplicates and plotted using the Hill equation.

Supplementary Tables

Supplementary Table 1. Tm values used. Related to Figure 1.

Species	Average Tm value (degree Celsius)
E. coli	54
T. thermophiles	79
S. cerevisiae	51
H. sapiens (Hela cells)	56

Supplementary Table 2. p53 homologs with low APR strength. Related to Figure 4.

APR or equivalent	TANGO score	UniProtKB ID	homology	species	% identity human p53 DBD
IRVVFRLI	0	A9UZX3_MONBE	p53-like	*Monosiga brevicollis* (Choanoflagellate)	34
MMQLHFTL	0	A0A0N5E6D9_TRIMR	p63	*Trichuris muris* (Mouse whipworm)	32
VYVDFSL	0	A0A0N4VCR4_ENTVE	p53-like	*Enterobius vermicularis* (Human pinworm)	31
TELEFTL	0	A0A195C1G0_9HYME	p63	*Cyphomyrmex costatus* (fungus breeding ant)	29
TELEFTL	0	A0A151XH99_9HYME	p63	*Trachymyrmex zeteki* (fungus breeding ant)	29
TELEFTL	0	F4X756_ACREC	p63	*Acromyrmex echinatior* (Panamanian leafcutter ant)	27
AIFTL	1,1	V5GSV4_ANOGL	p53	*Anoplophora glabripennis* (Asian longhorn beetle)	32
LIFNL	1,2	A0A154PH19_9HYME	p53	*Dufourea novaeangliae* (solitary bee)	31
IHTVF	1,8	A0A0L0G1F4_9EUKA	p53-like	*Sphaeroforma arctica* (*Opisthokonta, Protozoa*)	30
IIFHL	1,8	A8CSR7_NEMVE	p53-like	*Nematostella vectensis* (Starlet sea anemone)	35
LNAVF	2,0	Q4H300_CIOIN	p53-like	*Ciona intestinalis* (transparent sea squirt)	40
AIQLSITL	2,4	A0A0V0ZFM8_9BILA	p53	*Trichinella patagoniensis* (Nematode)	33
AIQLSVTL	2,5	E5SRY1_TRISP	p53	*Trichinella spiralis* (Nematode)	32
AIQLSVTL	2,5	A0A0V1GZU5_9BILA	p53	*Trichinella zimbabwensis* (Nematode)	31
TVFSL	4,3	A0A0A9W1L4_LYGHE	p53	*Lygus hesperus* (Western plant bug)	30
LNICFAL	4,4	F1L1F1_ASCSU	p53	*Ascaris suum* (Pig roundworm)	31
"ILTIITL"	**76**	**-**	**p53**	***Craniata***	**66**

Supplementary Table 3. p53 APR TANGO score and standard deviation per clade. Related to Figure 4.

Clade	N	TANGO score (SD)
Craniata	136	76 (13)
Mollusca	12	76 (9)
Diptera	57	53 (22)
Nematoda	25	36 (30)
Ixodida	8	35 (22)
Coleoptera	7	21 (21)

Supplementary Table 4. Selected mutations and codon usage. Related to Figure 4.

Mutation	WT codon	Mutant codon
L252K	CTC	AAG
T256R	ACA	AGA
A138G	GCC	GGC
R267L	CGG	CTG
N268D	AAC	GAC

Supplementary Table 5. Data collection and refinement statistics. Related to Figure 4.

	P53 charged core
Data collection	
Beamline	Proxima1 (Soleil, France)
Date of collection	10-Feb-2017
Wavelength (Å)	0.9786
Space group	$C222_1$
Cell dimensions	
a, *b*, *c* (Å)	68.42, 84.96, 84.85
α, β, γ (°)	90.0, 90.0, 90.0
Resolution (Å)	42.48-1.67 (1.73-1.67)*
R_{sym} *(%)*	8.2 (72.4)
R_{meas} *(%)*	8.6 (78.0)
$I / \sigma I$	17.2 (2.6)
$CC_{1/2}$ (%)	99.9 (83.4)
Completeness (%)	98.2 (95.1)
Redundancy	7.8 (7.2)
No. total reflections	222350 (19402)
No. unique reflections	28518 (2713)
Refinement	
Resolution (Å)	1.67
R_{work} / R_{free}	17.8 / 19.4
No. atoms	1866
Protein	1602
Ligand/ion	13
Water	251
Average *B*-factor	15.32
B-factor Protein	12.60
B-factor Ligand/ion	30.26
B-factor Water	31.89
R.m.s. deviations	
Bond lengths (Å)	0.024
Bond angles (°)	2.1
Ramachandran outliers (%)	0.0
Ramachandran favored (%)	99.5
Ramachandran allowed (%)	0.5

*Values in parentheses are for highest-resolution shell.